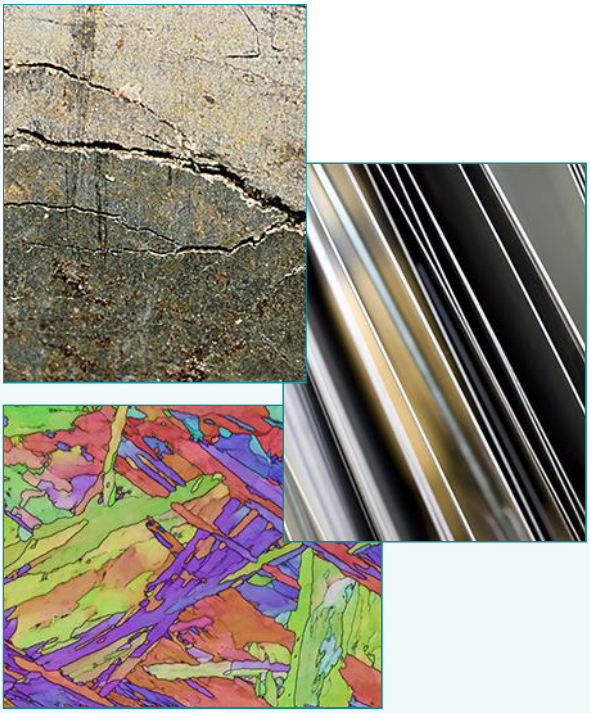

Research report

Open

In-situ X-ray radiographic quality control of 3D printed metal components

Erik Lindgren

Report number. KIMAB-2018-601

swerea | KIMAB

Title	In-situ X-ray radiographic quality control of 3D printed metal components
Authors	Erik Lindgren
Publication date	2018
Report number	KIMAB-2018-601
Status	Open
Project number	13374
Department	Material & Process Development
Research Area	Nondestructive Material Characterization
Member Research Consortium (MRC)	
Financing	Industrial
Distribution	Public
Approved by	2018-01-31

X TIS

Signerat av: Tania Irebo

Tania Irebo Schwartz

Group Leader

ISSN 1403—848X

In-situ X-ray radiographic quality control of 3D printed metal components

Erik Lindgren

Report number KIMAB-2018-601

Abstract

In this study techniques, setups, and procedures for in-situ (as built, layer by layer) X-ray nondestructive evaluation of metal components 3D printed with powder bed fusion or directed energy deposition have been explored. Mathematical models have been utilized in order to estimate the applicability of the proposed techniques. Simple experiments have been conducted in order to verify some, far from all, of the requirements and assumptions. Both the possibility to utilize the built in electron beam in the powder bed fusion electron beam melting machines as the source producing X-rays as well as well the option to utilize external X-ray sources for the case of the directed energy deposition processes have been explored. A proposed concept for backscattered X-ray imaging with an X-ray source has been simulated and seems promising for the application of in-situ layer-by-layer detection and depth positioning of small gas pores. A transmission X-ray imaging concept, less explored, has also been proposed.

swerea | KIMAB

Box 7047, 164 40 Kista, Sweden
+ 46 8 440 48 00, www.swereakimab.se

Table of contents

1 Introduction

Additive manufacturing of metal components in 3D (3D printing of metal components) is considered by many to become a major disruptive innovation in the manufacturing industry. The possibility to print complex geometry metal components with their geometry specified by a digital 3D CAD model will open up new possibilities. However, these new opportunities in the beginning and middle of the manufacturing process chain generate new challenges and difficulties later in the chain, especially at the quality control.

In many quality-critical industries (such as the oil and gas industry, nuclear, aerospace, and automotive industries) the quality of the manufactured component must be carefully controlled with so-called nondestructive evaluation. During the evaluation, the existence of defects that could potentially affect the desired properties of the component (for example the fatigue life) are identified and characterized. Typical defects of interest are pores, lack of fusion, cracks, and the characterization typically could address sizing and positioning. Much of the nondestructive evaluation currently requires a lot of manual labor and is carried out by skilled inspection engineers. The procedures and measuring equipment are carefully chosen and adapted for specific components, geometries and defects. The collection of measurement data can often be easily automated and digitized, but the automation of the preparation and analysis of the evaluation is more difficult to accomplish. However, this current methodology of nondestructive evaluation of manufactured products scales poorly with some of the major advantages of the additive manufacturing process, namely small series and complex component geometries.

Another major difference between additive manufacturing and conventional manufacturing processes is that in conventional manufacturing, the components are often quality controlled when finished. For example, welds are usually controlled after the entire welding process is complete. Any defects can then often be corrected by a small local welding or repair since the finished weld is often as easy to access as at the first welding. A local repair is carried out rather than scrapping the entire component. However, this does not in general apply to additive manufacturing which in sense is one large weld itself. Defects found in the internal volume of the finished product are in general difficult to repair and the entire component must often be scrapped if critical defects are found in the finished component.

We do believe that another approach to nondestructive evaluation of 3D printed metal components is required: one that neither requires intense manual labor nor results in scrapping finished components. We propose that in-situ, as the component is built, nondestructive evaluation of the quality of the component could be part of such an approach. Such an approach would facilitate the correction of defects during the build process (less scrapping) as well as facilitate the automatization of the evaluation by dividing the evaluation problem into less complex sub-problems.

In this project the possibility to use X-ray inspection and tomography for in-situ, as the component is built, quality control of 3D printed metal components has been mainly theoretically explored. The idea behind this project was that customized reconstruction algorithms and X-ray inspection procedures could be developed which actually tried to make good use of the additive in the manufacturing method, that is, the fact that geometric complexity goes from low to high as more and more of the component is built and that the inspection could be conducted incrementally.

The vision was to obtain a high degree of generality of the evaluation by naturally dividing the problem into simple sub-problems, that is, the evaluation is general in the small but the sum is complex. The idea was to get inspiration to the new custom reconstruction algorithms from 3D-point reconstruction [1, 2] and dynamic tomography [3].

In-situ nondestructive quality control of the 3D printed metal components is not a new idea. A few earlier studies on this subject will be reported later in this work. However, in-situ X-ray inspection of 3D printed metal components is rather unexplored.

The part of the overall described problem that will be addressed in this work is therefore the automatization and digitalization of the inspection and its preparations, to some extent also the data analysis. The scrapping problem is address rather by the fact that such an in-situ nondestructive evaluation would facilitate the local repair of the component as defects are sprung into existence during the build. This project is thus intended to take one small step further towards an unbroken digital chain between the design idea and a finished nondestructive quality controlled 3D printed metal component.

In this report almost all of the work that has been done in this project will be reported, both the successful and the un-successful work. First some background will be given, describing briefly the additive manufacturing processes of interest. A review of the state-of-the-art within nondestructive evaluation, especially in-situ, of 3D printed metal components is reported. Nondestructive quality control with X-ray inspection is also briefly explained since it is central to the work. Based on the background some inspection procedures and potential algorithms will be defined and the inspection then simulated. In addition, some small well defined questions in connection to the proposed procedures have been experimentally explored. The report is finished with conclusions.

1.1 Project plan

The project was divided into four work packages in the project funding application. For completeness they have been translated into English and written down in this context.

Work package 1: Component geometries

Industrially relevant simplified component geometries, primary for the aero industry, are defined. From earlier collaborations with for example GKN Aerospace Engine Systems in Trollhättan Sweden the project group already have sound knowledge about defect type and sizes (for example pore and lack of fusion defects) critical to the quality of the component (for example the fatigue life properties).

Deliverables: geometry and defect specifications.

Work package 2: Simulated X-ray inspection

Simulations of in-situ online quality control with X-ray computed tomography of 3D printed components are produced in order to evaluate the proposed quality control and algorithms. Input to the simulations, the component geometry and defects, is taken from work package 1. Already existing models and implementations that have already been validated is utilized for the simulations [4, 5]. Modifications are made in the models and implementations in order to adjust the models to the specific application.

Deliverables: Synthetic radiographs.

Work package 3: Conceptual procedure and algorithm development

In parallel with the simulation of the in-situ quality control algorithms are produced for the nondestructive evaluation. The methodology to start the development of analysis algorithms by utilizing realistic simulations of the inspection has proved successful earlier [1, 2]. That is, the concept with an iterative algorithm for in-situ volumetric reconstruction of the component and relevant defects are explored at this early phase with simulations.

Deliverables: A proposed inspection procedure and algorithms, and if relevant a scientific publication draft.

Work package 4: Report writing

Produce a compilation of the results and to write a report.

Deliverables: Project report.

2 Background

In this section a brief background will be given, and the reader is assumed to have general knowledge within the field of the report. The additive manufacturing processes of interest will be conceptually described and the critical manufacturing defects of interest specified. This will be followed by an introduction to X-ray radiographic nondestructive evaluation. When selecting defects of interest for and when exploring the X-ray based methods, the capabilities with respect to the specific applications of other than X-ray based methods are of interest. Therefore, a literature review covering methods, including other than X-ray based, for in-situ quality control of 3D printed metal components will be reported.

2.1 Additive manufacturing

There exists a large number of additive manufacturing methods, however in this report only the following methods are considered: powder bed fusion with an electron beam (PBF-E) and a laser beam (PBF-L), and directed energy deposition of powder (DED) with either a laser or an electron beam. Powder DED (in this context abbreviated DED even though there exist other material feeding approaches than powder, for example wire) is in the case of a laser beam also known as laser blown powder and laser powder deposition. All these methods are actively explored for manufacturing components in quality concerned industries such as for example the aero industry. In addition, in this report only additive manufacturing of metal parts or components is considered. For a more in depth introduction to thus subject, see for example [6].

In powder bed fusion the powder is applied iteratively layer by layer over an area that spans the largest possible outer limits of the finished 3D printed component which is limited by the build tank (see Figure 1). The powder application is followed by selective melting, in this case with either a laser or an electron beam. Obviously, in relevant cases, not all powder is melted and the finished object is made up by the melted regions. The un-melted (in the PBF-E case slightly sintered) powder is left, side by side to the full melted regions and the build platform (see Figure 1) is lowered and another layer of powder is applied. That is, the semi-finished structure is embedded in powder.

Figure 1. Photograph of the interior of a PBF-E machine from Arcam. Left) build process chamber with the build platform encircled in red, right) the build tank which is positioned over the build platform, wall thickness around 10 mm, in order to keep the powder in position.

The principle described above is the same for both the electron as well as the laser beam PBF machines. However in detail PBF-L and PBF-E differs. The layer thickness is around 20-60 µm in PBF-L machines and around 50-70 µm in PBF-E machines. In addition, in the PBF-E case the build surface is typically held at elevated temperature, the actual temperature depends on the material grade, but around 1000 degrees Celsius is not uncommon, and the powder is sintered together into electrical contact prior to the actual melting. Another notable difference between PBF-E and PBF-L is that the electron beam as it impinges on the build surface is actually producing X-ray photons. The setup is similar to an industrial X-ray tube and an X-ray source therefore already exists in the electron beam machines. The electron gun in commercially available systems from Arcam typically operates at 60 kV with a minimum spot size around 100 µm and a maximum power of 3 kW. Also, recently Arcam introduced an X-ray detector as an add-on to their PBF-E machines. For details in the PBF-E build process see [7] and for details on the machines see the webpage of the machine manufacturer Arcam (to the best knowledge of the author Arcam is the only available manufacturer of electron beam melting PBF machines).

As a rule of thumb around 2-3 layers are often said to be re-melted each time a new powder layer is added in PBF. Therefore a relevant depth from the build surface where defects should be detectable (if inspected between each new layer) is for example in the PBF-E case around 100-200 µm. The exact depth depends on the process parameters and the materials involved, see for example [6] for further details.

In the directed energy deposition methods powder is blown out (or wire is applied) and applied only local where the laser or electron beam is instantaneously melting the powder, line by line, layer by layer. In this case, ideally, the semi-finished structure is not embedded in powder. Typically the nozzle or wire feeder is applied on an industrial robot. The thickness of each layer is around 0.3-0.5 mm deep and the melt pool is around 0.1-0.5 mm in depth [6], that is, around 1 mm of depth should be inspected for defects per applied layer. As stated in [6], each track is also overlapped with the previous by approximately 25 %.

2.1.1 Critical manufacturing defects

In this section the relevant defects for the selected additive manufacturing processes is described. The defect type, orientation and size influence the choice and the preparations of the nondestructive evaluation method. The list of defect types is not complete but rather represents an example of common critical manufacturing defects, critical in the sense of affecting the structural integrity or the fatigue life of the components. Also, in this context the focus will be on the defects, however as noted in most cited works, by careful optimization of the process parameters the components can be successfully built with the selected processes.

Many of the references in this section were found in [8] which is a literature review of the correlation between the PBF process parameters and the manufacturing defects in nickel-based super-alloys commonly used in the aero industry.

Considering first the PBF-E 3D printing of nickel-based super-alloys. In [9] cracks and binding faults could be detected in cross sections with optical microscope and scanning electron microscope (SEM). The elongated binding faults, similar to irregular shaped porosity, were in the size interval 50-500 µm and with the length to width ratio approximately 10:1. Cracks around 100 µm were also reported. In [10] spherical porosity was observed in cross sections with SEM analysis, the porosity was arranged in strings perpendicular to the layers. So called process-induced porosity much less spherical in shape compared to the gas porosity could be observed in [11]. The process-induced porosity was elongated in parallel with the build layers, the size in the elongated direction was around 400 µm as measured in one of the figures in the article, for details see also [12].

Similar manufacturing defects occur in the PBF-L process. In [13] SEM and synchrotron tomography were utilized to detect two different void types in printed Titanium-6Aluminium-4Vanadium (Titan-64): spherical pores larger than 50 µm; elongated narrow crack-like voids oriented in parallel with the layers, typically longer than 100 µm and similar to lack of fusion defects. In [14] tensile strength and creep tests were applied on printed nickel-based alloy samples. Post-processing, high isostatic pressing (HIP) was applied in order to close micro cracks and void defects. SEM was utilized to identify 50-250 µm cracks some 0.5 to 2 mm apart. The embedded cracks could be closed with HIP but not surface reaching cracks. Porosity, not only spherical, in the rage 50-500 µm was also reported.

Solidification cracks (around 100 µm) from the PBF-L process, irregular shaped bonding defects around 50 µm and spherical shaped pores in nickel-based super-alloys were reported in [15]. The size of the porosity was taken from cross section characterization, and thus will possibly not indicate the largest defect present. The cracks propagate along the grain boundaries in the build direction and are believed to be initiated as solidification cracks. The crack and pore formation is shown to have an inverse relationship.

As for the Powder DED (laser) case similar to the PBF case lack of fusion and spherical pore defects have also been reported. In [16], the deposited Titan-64 contained lack of fusion defects which were elongated in parallel with the layers, lengths of around 300 µm can be seen in the article. Similar findings were reported in [17] where 200 µm spherical pores and lack of fusion defects were found in deposited tungsten-rhenium alloy (utilized in for example structural components in the nuclear industry). The lack of fusion defects were irregular in shape and void-like, positioned between the layers, and extending up to 700 µm in length and with the width varying from almost not visible to 200 µm.

In most practical cases the 3D structure is built on top of a substrate which is removed from the structure when it is finished. However it is not always removed, especially DED has been proposed as a method to repair components already in service, see for example [18]. In [19] a repair method was evaluated in which a critical defect was removed from a component (substrate-like) by grooving and the grove was repaired by filling material with DED-L. In the deposited material irregular shaped void defects (some around 1-2 mm in size) typically at the interface between the repair and the base material was found.

2.2 Nondestructive evaluation with X-ray radiography

In this section nondestructive evaluation with digital X-ray radiography will be described. The matter will only be dealt with very briefly, in order for readers with different backgrounds to be able to read this report. For a more in depth description of nondestructive evaluation methods see for example [20] and for a more in depth description of digital X-ray inspection se for example [21].

Essentially there are two different modes of operation in industrial X-ray radiography, transmission and backscatter imaging. The principle of transmission imaging is straight forward (see Figure 2): a 3D volume is projected onto a 2D plane, the detector; high energy X-ray photons are emitted by a source, the photons interact with the object to be inspected which is positioned between the source and the detector, and the photons that are not absorbed or too much scattered are detected at the detector. The detected signal will thus contain photons that passed through the object without interaction and scattered photons. The spatial distribution in the detector plane of the scattered photons is in general much more difficult to model as a function of the material and density variation in the object, and is therefore often considered information degrading and not of interest. Industrial nondestructive evaluation conducted with transmission X-ray imaging, as a broad category, is an often used and mature technology with international standards readily available describing for example weld inspection.

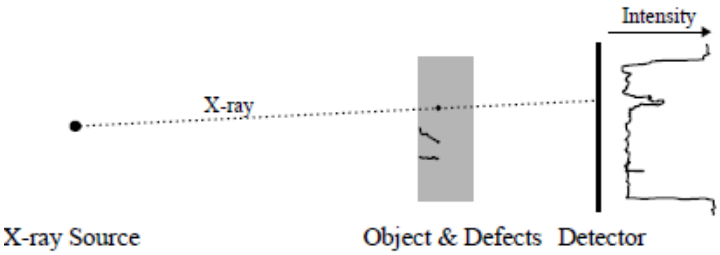

Figure 2. Illustration of transmission X-ray imaging, included with permission from [21].

In backscattered X-ray imaging only the scattered photons are instead detected. There are different procedures available but the overall concept is illustrated in Figure 3. The X-ray photons emitted from the source interact with the object to be inspected, some of the photons are scattered in directions leading out of the surface again where they can be detected. The number of scattered photons in different directions and their energies depend on the material and the density of the volume of the object. Compared to transmission imaging backscattered imaging does not require access to both sides of the object.

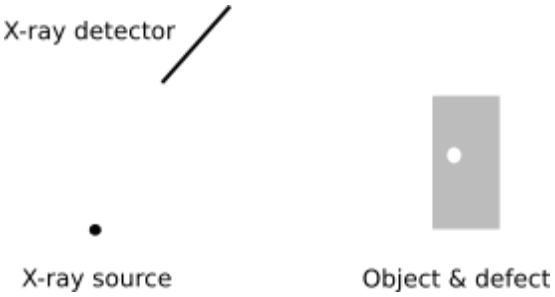

Figure 3. Illustration of backscatter X-ray imaging.

Image quality is a central concept within industrial X-ray radiography, and there are ISO and ASTM standards describing how to qualitative and quantitative estimate it with so called image quality indicators (IQI), see for example SS-EN ISO 17636-2. Both the contrast, often taken as the contrast to noise ratio which is the difference between two signals (for example the background and the indication) divided by the average noise level (typically the standard deviation), and the resolution are important. The contrast can be estimated with for example hole type IQIs, which is a plate with specified material, thickness and hole diameters. The resolution is instead estimated with duplex wire IQIs, containing pairs of thin closely spaced wires.

The signal that is formed in X-ray radiography is intrinsically random by nature. The generation, interaction with the inspection object, and the detection of X-ray photons are all random processes. The uncertainty in the signals is typically decreased if averaged over time, the so called exposure time. Therefore, the combination of a high intensity of the X-ray source together with a fast readout (to average also over the consecutive readouts) low background noise digital detector is often of interest to reach low exposure times and high contrast to noise ratios.

Next, having dealt with the conceptual and practical parts of X-ray radiography, a short theoretical background to electron and photon interaction with matter will be given. A set of relevant interaction types will be described (based on [21]) since they are referred to in the results of this report. For further details see [21] and some standard textbook for example [22].

As an electron is transported in matter its energy is decreased. In the context of this report the most important interactions are elastic scattering, in-elastic scattering, and bremsstrahlung. In elastic scattering the electron is deflected but loses approximately no energy. In in-elastic scattering the electron will instead both be deflected and lose energy. The energy loss goes into a new free electron and to excite or ionize the atom. The atom will relax to its ground level by for example emitting a characteristic energy photon. In for example Titanium (similar to the Titan-64 alloy common in the aero industry) up to energies of a few 100 keV the elastic scattering is the most common, at 100 keV elastic scattering will take place on the average every 20 nm and in-elastic every 50 nm. The third interaction of interest is the bremsstrahlung, which consists of photons that are emitted as the electron brakes into matter. The emitted photons have a smooth continuous energy distribution and the angle distribution depends on the electron direction, the atomic number (Z), electron energy and the energy of

the emitted photon. In conventional X-ray tubes, it is the bremsstrahlung that is mainly utilized as the output X-ray beam.

In this report there are three relevant types of photon interaction with matter: elastic (Rayleigh) scattering, inelastic (Compton) scattering, and photoelectric absorption. In Rayleigh scattering the photon is deflected without any energy loss. The distribution is overall peaked at small deflection angles. In photoelectric absorption the incoming photon will ionize the atom and leave behind the atom with a vacant energy state together with a free electron. The atom will relax by emitting characteristic energy photons or possibly an Auger electron. The angular distribution of the photoelectron is non-trivial.

Finally, in incoherent scattering of the photon it will change its direction and energy, and ionize an atom which will eject a free electron. The angular distribution of the scattered photon around 100 keV and relevant materials is not negligible in the backward direction.

2.2.1 Backscattered X-ray imaging

Backscattered X-ray imaging will be central to the results in this report. Therefore its state-of-the-art and somewhat more details were included in this report.

For the relevant X-ray energies in this context Compton scattering will be the dominating interaction producing the backscattered image (radiograph). As stated in the recent review on the technique in [23], Compton backscatter imaging can be divided in four different setups: point-by-point, line-by-line, plane-by-plane, and energy-coded imaging, see Figure 4.

In point-by-point imaging the source and detector both are collimated, only emitting and accepting X-rays in a very narrow angle interval. The intersection between the source beam and the detector (single pixel) angle window represent a sub-volume in the object to be inspected. Sub-volumes at different depths can be inspected by moving the detector and sub-volume at different lateral positions by moving both the source and the detector.

In the line-by-line imaging the single pixel detector is replaced by a 1-D linear detector array. Sub-volumes at different depths can thus be inspected without moving the detector as they will be imaged on different pixels in the detector array. The principle was implemented into a commercially available product which is currently marketed by Yxlon (www.yxlon.com), the ComScan system. The ComScan was designed for a maximum depth of view at 50 mm and a resolution at 0.5 mm and utilizes two linear detectors, one on each side of the source ray.

In plane-by-plane imaging, also known as the pinhole camera, the source is un-collimated and the backscattered X-ray photons are collected with a 2D digital detector array (DDA) where a pinhole is positioned between the detector and the object. However, the depth position of the detected signals (indications) is difficult to obtained, at least not at a high accuracy, and in [23] it is argued that it is similar in efficiency (total inspection time of a given volume) as the line-by-line imaging setup.

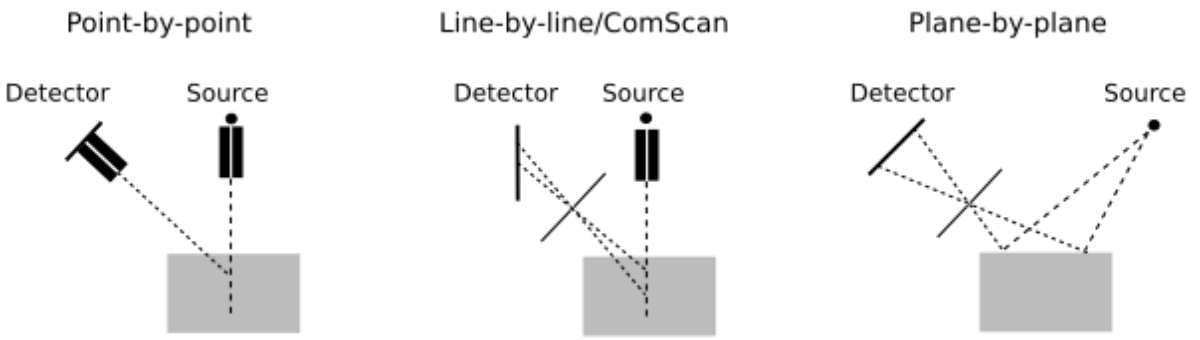

Figure 4. Illustration of different setups for backscattered imaging.

Finally the energy-coded scattering imaging is listed in [23] which based on measuring the energy of the detected X-ray photon which together with mathematical models of the relation between the scattering angle and energy will yield the deflection angle and origin of each detected X-ray photon. A monochromatic collimated source is required and so far the reported spatial resolution is low at around 1 cm.

A point-by-point setup was successfully used in [24] to detect and size artificial cracks (2 x 0.02 mm slits) behind up to 4 mm of steel. A source voltage of 200 kV (the maximum emitted photon energy is therefore 200 keV) was used to detect the artificial crack behind 2 mm of steel, 300 kV for 3 mm, and 320 kV to detect the artificial crack behind 4 mm. The detector was a scintillator crystal connected to a photomultiplier, both source and detector collimators had a slit width of 0.5 mm. The setup was later modified to include a multi-slit collimator (219 holes) on the detector and demonstrated [25] to be useful for wall thickness measurements and delamination detection. The thickness measurements were shown to have an accuracy of 0.01 mm of 11 mm thick carbon fiber. Delaminations as thin as 0.05 mm, perpendicular to the source ray, were detected in 2.5 mm thick carbon fiber component.

In [26] a plane-by-plane setup was utilized to successfully detect artificial cracks (slits 1 x 0.05 mm) in stainless steel at a depth of 0.7 mm (metal oxide coating, 1.2 g/cm$^{3)}$. An image intensifier connected to a CCD camera with 50 µm pixel size was utilized in combination with a 80 kV/4mA cone beam X-ray tube. An exposure time of 5 minutes was required and different pinhole configurations were explored.

A special form of collimator, a twisted slit, was explored in [27] in combination with an un-collimated source. A standard digital detector array (DDA) with pixel size 143 µm was utilized for the detection and the purpose of the twisted slit collimator was to project different locations on the object onto different pixels on the DDA. The purpose with the setup was to lower the required exposure times, improvements from hours down to 3 mm was demonstrated. A high energy X-ray source operating at 450-600 kV was utilized. The detection of water in honeycomb structured plates as well as small thickness variations in a heterogeneous (5-65 mm) aluminium component was demonstrated. In [28] the collimator was further developed into a twisted multi slit collimator. The development of the required analysis algorithms, for constructing a single radiograph of the multiple projections, was conducted with simulated radiographs.

2.3 Nondestructive evaluation of 3D printed metal components

In this section the state-of-the-art of nondestructive evaluation of metal components built with the selected subset of additive manufacturing methods, PBF and DED, is presented. Focus is on in-situ evaluation (while building the component layer by layer) but some post-build evaluation (after the whole component has been finished) studies are also included.

Most of the in-situ studies were not actually experimentally performed in-situ, but rather with a setup simulating an in-situ inspection and with a stated aim of in-situ evaluation. In-situ nondestructive evaluation is emphasized since it is believed to be critical in many applications in order to: handle the complex geometry of the 3D printed parts and in order to facilitate in-line correction/repair of the printed parts.

This section has been split up into four sections: 1) in-situ pyrometry, thermography, and vision systems (the most explored methods for in-situ evaluation); 2) in-situ ultrasonic and laser ultrasonic methods, which have recently gained increased attention; 3) in-situ eddy current; 4) post-build methods, where X-ray computed tomography is the most explored method.

2.3.1 In-situ pyrometry, thermography, and vision systems

Pyrometry, thermography, and vision systems are the most explored in-situ nondestructive evaluation and process monitoring methods for AM. In pyrometry the temperature of a surface is measured contact less by measuring the emitted radiation from the surface. Thermography is similar but an image of the radiation of the surface, typically in the infrared regime, is collected and analyzed. The vision systems typically operate in the visible wavelength range of the electromagnetic spectrum with a camera. It is essentially digital visual inspection with the aim of being automatic. For an introduction to thermography and visual inspection, see for example [20].

Many of the PBF and DED machine manufacturers offer a camera based solution, for example Arcam, Concept Laser, and EOS all have camera based in-situ process monitoring included in their machines. In most cases the melt pool is monitored and its behavior connected to for example the existence of pore defects. However, in the Arcam case, the pore defects are claimed to be detected directly rather than indirectly.

In a recently published review article [29] it was concluded that for PBF visual camera based methods have been used to identify processing errors and closed-loop control with pyrometry in order to keep the temperature gradient across the surface constant. However, the harsh environment in the build chambers, licensing and patent issues were pointed out as limiting the machine integration. As for DED, closed-loop feedback utilizing camera based vision systems has been demonstrated. It was also concluded that the development of sub-surface inspection methods (most methods to date are only surface methods) with higher resolution are required.

In [30] pore defects down to 0.1 mm were detected in the PBF-L process by measuring the melt pool shape and temperature. The PBF-L setup was an in-house developed setup at KU Leuven. A photodiode and a near-infrared CMOS camera was set up coaxial with the melting laser beam to detect light in the wavelength interval 0.8 to 1 µm. A sample rate at around 10 kHz was achieved, with the possibility of real time process feedback. The experimental

results were shown to agree well with X-ray CT measurements of a cutout of the built samples.

As pointed out in [31], most of the thermography approaches have been based on measuring relative temperatures rather than true temperatures. In order to measure the true temperatures hyperspectral imaging with multiple IR images collected at different wavelengths was proposed in [31]. The measured intensity versus wavelength, as well as the peak intensity, ideally follows a well-known law which would be utilized. It was argued that also the emissivity should be possible to measure simultaneously. The equipment was planned to be mounted outside of the chamber of an EOS PBF-L machine.

A bolometer thermal camera, mounted off-axis outside of the chamber of an EOS PBF-L machine, was utilized to detect void defects in Inconel 718. The defects were made intentionally as powder filled un-melted regions. An effective resolution of 0.25 mm was achieved with lenses. The detection limit of the voids was around 0.3 mm in size and depths down to about the same as the size of the void could be inspected. Several different indication scalars were extracted from the images: thermal diffusivity, an indication of the effective heat dissipation over an extended time; time above a given temperature; number of sputtered particles; maximum temperature. The problem with varying emissivity was elaborated on in the article but it was not clear to the author exactly how the emissivity was used in order to get the temperature readings. Therefore it is assumed that temperatures stated are given at an assumed constant emissivity. Repetition rates in the Hz-regime was achieved, typically too slow for inspection of the whole surface. However, as proposed, the method could perhaps be useful for inspection part of the build surface and for increased understanding of the processes.

In [32] a visible light (around 0.9 µm) high resolution (0.1 mm) CMOS camera was mounted on a PBF-L machine for defect detection. Fabricated defects (most probably un-melted spheres) down to 0.3 mm in size were detected; defects down to 0.05 mm could possibly be discerned but seemed to be very similar to noise. An area of 250 mm^2 could be captured at 0.1 mm resolution and 100 Hz.

A high speed and high magnification setup for thermographic melt pool monitoring in a PBF-L system was developed in [33]. The purpose was to compare the melt pool dynamics with simulations. The optics was mounted outside of the machine, and the wavelengths between 1-2.5 µm selected for detection. The melt pool, defined as the spatial region above 500 degrees Celsius (Inconel 625), captured with about 35 pixels, was sampled at 1800 scans per second. Hot particles in the size range 100-200 µm, ejected from the surface, could be detected. For measurement of the true temperatures they referred to [31], which was a conceptual proposal for true temperature thermography.

Thermography of the PBF-E process is complicated by sputtered metal particles which might coat the surface of the sensor or in other ways interfere with the measurements. In [34] a sacrificial Mylar film was utilized to protect an infrared camera (1.5-5 µm) mounted inside the machine at a process chamber viewing hole. The concept of the Mylar film protection was successful and pore defects were claimed to be detected. However, some other verification (destructive or for example X-ray CT) of the existence and size of the pore defects was lacking.

There are still issues with the three listed methods. For example, the vision systems are all highly limited to surface defects, and as already pointed out the thermography methods are all

limited to surface close defects. An increase in resolution is required, and in combination with large inspection volumes, the inspection speed is also an issue. In addition, both the pyrometry and thermography methods suffer from the uncertainty in emissivity. The emissivity relates the radiated energy to the surface temperature and typically depends on many factors such as: temperature, surface roughness wavelength, source roughness, view angle; thermal noise from the surroundings, see for example [35] or [31]. Nevertheless their applicability as part of a solution is most probable.

2.3.2 In-situ ultrasonic and laser ultrasonic testing

Ultrasonic nondestructive evaluation is a mature, readily available and heavily utilized inspection method within many quality concerned industries. International standards describing for example weld inspections exist. In conventional ultrasonic inspection typically a piezo electric probe is used to transmit and receive the mechanical waves introduced into the object to be evaluated. The probe must (at least in the applications relevant in this context) be in direct contact with the surface of the object and a coupling medium, for example water or gel, must be used. The mechanical waves interact with the test object and for example defects will reflect or attenuate the waves which are detected with the same or a similar probe on the surface of the object. The ultrasonic wave propagation and interaction is sensitive to a multitude of material properties, which can potentially be measured.

Instead of generating and detecting the ultrasonic waves with a piezo electric transducer a high energy lasers can instead be utilized. Laser ultrasonic offers potentially higher spatial resolution and fewer requirements on the accessibility, since the laser spot is much smaller than the piezo electric transducer. In addition, it is contact less. These properties are suitable for in-situ nondestructive evaluation of additive manufacturing, and have recently received quite a lot of attention within the research community. It is however not trivial, the measured signals are often both weaker and more complex than in conventional ultrasonic evaluation. It is out of the scope of this text to offer an introduction to neither laser ultrasonics nor ultrasonics, see for example [36] or [20] for ultrasonic inspection and [37] for an introduction to laser ultrasonics.

The first attempt that has been found on using conventional ultrasonic testing was found in [38]. A piezo electric transducer was mounted on the bottom of the build platform in an EOS PBF-L machine. A simulated lack of fusion (2 mm, produced with 25 % of laser power) was detected. In addition, a 2 mm sphere (filled with un-melted powder) in a 10 mm thick cylinder could be detected as a reflected wave echo, but the signal was rather noisy. Since ultrasound was generated and detected from the bottom of the build, complex geometries can probably not be inspected. A similar approach was proposed and planned in [39]. However that study aimed at correlating the ultrasonic wave speed of the back wall echo with the porosity level in the build.

An early attempt on utilizing laser ultrasonic for inspection of laser cladded material, a process very much similar to DED-L, can be found in [40]. Artificial defects, flat bottom EDM (Electronic discharge machining) holes, 0.5-1.5 mm in size positioned 0.4-0.8 mm from the surface was fabricated in titan-64 and stainless steel. Small laser spot sizes, 0.1-0.3 mm, together with a generation detection distance at around 1-3 mm was set up. The indication of interest in the signal was a broadening (over time) of the Rayleigh surface wave, produced by shear or pressure wave which was mode converted on the surface shallow defect. The

detection limit was at the 1 mm defect, possibly with false calls, and a wavelet filtering approach was required.

Laser ultrasonic was one of the methods explored for in-situ evaluation of DED-L in [41]. In-situ was the aim but the experiments were rather conducted in close proximity to the DED setup. Both samples with artificial, hole diameters 0.1-0.7 mm, and process induced defects were used. The surface Rayleigh wave was again used, but a decrease in the amplitude was used as the defect indication. An approximated probability of detection (POD) at 90 % for 0.1 mm surface close defects and 0.9 mm at depth around 1 mm could be achieved. Near surface flaws in the sample with the process induced defects could also be detected, typical size around 0.5 mm was quoted.

Samples made of Inconel 718 and Titan-64 fabricated with powder DED-L, wire DED-L, and wire DED-E processes, were evaluated with laser ultrasonic inspection in [42]. Compared to X-ray CT on cutouts, the detectability limit was 0.4 mm for porosity in the powder sample and lack of fusion defects were detected in the wire samples. The experiments were conducted off-line but with in-situ as the aim. It was found that inspection from the top side (probably necessary for in-situ) resulted in a considerable better defect detectability than from the machined substrate side (bottom). The ultrasound that was reflected off the defects were used, as well as the synthetic aperture focusing technique (SAFT) in order to increase the effective signal to noise ratio of the indications. In SAFT the same defect indication is tracked in several scanned positions on the surface, with a set of simple assumptions on the material, and knowing the sound velocity in the material an average with better statistics can be constructed, see [43] for details.

In [44] Inconel samples fabricated with DED-L, containing both fabricated artificial defects (Laser machining and EDM) as well as process induced defects, were evaluated with laser ultrasonic inspection. Both the ultrasonic surface waves and the bulk waves were considered. The ultrasound was generated in the thermoelastic regime with 1 mm of a separation between the generation and the detection spots. The detectability limits were, with qualitative analysis of the B-scans: for artificial defects, 0.1 mm if positioned close to the surface (around 0.4 mm) and larger sizes if at larger depths; for process induced defects, 0.5 mm detected at a depth of 0.4 mm but not at a depth of 0.7 mm.

Laser ultrasonic inspection has recently also been explored on samples printed with the PBF-L process. In [45] Titan-64 samples with EDM holes 0.6-1.3 mm at depths 0.25-1.3 mm was evaluated off-line but with the aim of in-situ evaluation. The surface Rayleigh wave was utilized as the indication of interest, and a generation detection distance at 3 mm together with a small 0.2 mm detection spot size. In total 41/48 defects are found, all the ones with a diameter above 0.73 mm, and all at less 0.7 mm depth. In [46] the same research group conducted similar experiments but with printed spherical powder filled holes instead of EDM holes, 0.2 mm in diameter at 0.25 and .5 mm below the surface. Again the surface Rayleigh wave was utilized, however the indications were much more unclear than in the EDM case and not detected. The existence of the powder filled defects could not be verified with X-ray CT, however the CT inspection required for detecting such defects could be difficult to set up. Two surface close spherical pores, around 0.7 mm in size, could be detected with the laser ultrasonic setup.

In conclusion, conventional ultrasonic inspection seems difficult to utilize in in-situ nondestructive evaluation during the build. The laser ultrasonic evaluation results look more promising, but issues remain with the build surface roughness and defect size detectability limit. Since the surface roughness is at similar length scale as the defect sizes it is difficult to utilize the existing contrast enhancing algorithms with high efficiency.

2.3.3 In-situ eddy current testing

Another possibly applicable method for in-situ nondestructive evaluation of 3D printed metal components found in the literature is eddy current testing. Its high sensitivity for surface close defects, contact less mode of operation, and high technology maturity makes it interesting. Eddy current testing is based on electromagnetic induction. Its working principle is: an alternating magnetic field is created in the vicinity of the object that is to be evaluated (must be conductive), the object will respond by setting up (eddy) currents in order to generate an opposing magnetic field. Defects will have an effect on the conductivity and permeability of the object, which will in turn have an effect on the impedance of the, for example, coil in the detection probe. For further details, see for example [20].

In [41], among other methods, the applicability of eddy current testing was explored. Powder DED-L was used to produce samples with both artificial and real process defects. A 90 % probability of detection for surface close defects was achieved at 0.2 mm defect size, and at 1 mm of depth at a size of 0.6 mm. The surface condition of the sample containing real defects at the time of eddy current testing, machined or not, was a bit unclear. It should also be noted, that a patent [47] do exist for an on-line nondestructive evaluation concept based on eddy current (or laser ultrasonics or electromagnetic acoustic transducer).

2.3.4 Post-build nondestructive evaluation

Nondestructive evaluation of the finished objects (post-build) is a potentially broad literature review since it typically includes also studies not related to additive manufacturing at all. The subject is included in this work only due to its relation to the in-situ evaluation and the review will be far from complete and contain rather a few examples. The emphasis will be on the potential issues with X-ray based methods (including X-ray computer tomography (XCT)), for example the defects which are potentially filled with un-melted powder as compared to gas filled.

X-ray computed tomography (XCT) has been explored in a large number of studies on internal defects in additive manufactured components. A recent review on XCT as a nondestructive testing method for verification of the quality of AM parts is given in [48]. The review points out that XCT has been successfully utilized to measure: porosity, with results compared to the Archimedes method (density based), however the porosity distribution within the volume cannot be determined with Archimedes method; the surface texture or roughness in the interval 5-30 µm, with results comparable to optical and contact methods; dimensions of outer and inner geometries. Standard reference samples and procedures to reliably approximate the uncertainty in the measurement results are however lacking, both for porosity and dimensional measurements. The issue with the uncertainty approximation of the measurement results is addressed in for example [49] and [50]. The review concludes that a high detectability of fatigue critical defects typically requires the samples to be cut-out (destructive), due to the well-known XCT issue that the resolution in the measurements depends on the density and the size of the sample.

In [51] XCT was utilized to measure the size of internal and external spheres and half spheres in Titan-64 samples fabricated with PBF-L. The outer size of the object was around 20 mm. The object was intentionally made to include internal and surface breaking half spheres in the diameter range 0.25-10 mm. The difference in size as measured with XCT and a coordinate measurement machine (only surface breaking spheres) was found to be around 2 %. The radiographical contrast of the internal spheres, filled with un-melted powder, was enough to be used in the size measurements. The comparison of the XCT results with the design intentions (CAD) showed increasing deviations with decreasing size, 5 % at 1 mm and 40 % at 0.25 mm.

The applicability of transmission X-ray imaging for the detection of defects in PBF-L printed Hastelloy X (nickel-base alloy with a density similar to Inconel at 8.2 g/cm^2) has been explored in [52]. Internal features in the shapes of rods, spheres, and coins were fabricated (by design) in the object. The authors pointed out that the X-ray attenuation versus the photon energy would only differ by a constant in the un-melted powder regions inside the defects compared to the melted base material. Conventional analog X-ray radiography was compared to digital computed radiography (CR) and XCT. (In CR a phosphor plate is exposed to X-ray photons and brought to scanner unit which activates the phosphors with laser and scans the visible photons, the distribution of the visible photons are digitally recorded and the output the radiograph). The resulting detectability limits: with conventional radiography, 0.2 mm spheres could be detected in up to 5 mm thickness; with CR, 0.2 mm spheres in up to 2 mm thickness, and 0.4 mm spheres in up to 5 mm; with XCT, 0.2 mm spheres could barely be detected at the voxel size of 0.12 mm where the large voxel size was required due to the large size/density of the object. The possible applicability of X-ray phase contrast imaging (highly sensitive to interfaces, including interfaces perpendicular to the beam direction) is proposed for future exploration.

In [53] Titan-64 wire and powder DED-L samples were evaluated with ultrasonic inspection (water flow focused probe), analog radiography (with conventional X-ray tube), computed radiography (with micro focus X-ray tube), and eddy current inspection. Defects of interest were lack of fusion, cracks, pores, and inclusions. In addition to intentionally made lack of fusion defects in the samples, artificial flat bottom holes were also made with diameters 0.4, 0.8, 1.2 mm at a depth of 3 mm in a material thickness of 2-42 mm. UT required the surface to the machined prior to evaluation. The resulting detection limits for the flat bottom holes were: UT, 0.4 mm in 42 mm; CR, 0.4 mm in 22 mm; Analog radiography, 0.4 mm in 44 mm. The lack of fusion defect was not detected with the X-ray methods, probably due to misalignment of the source with the defect. The eddy current evaluation capability was explored on artificial defects made with EDM instead, approximately 1x0.05 mm at depths 0.3-1.9 mm. The depth limit for detection was found to be around 1-1.6 mm, but thought to be more cumbersome with complex geometries.

3 Proposed inspection procedures and setups

In this section, based on the above literature surveys, a few different X-ray inspection procedures for in-situ evaluation of the selected AM processes will be proposed. Specific questions to be answered with simulations and a very limited set of real radiographic experiments will be defined.

Crack-like defects are in general more difficult to defect with X-ray based methods rather than with for example ultrasonic methods, or in the case of defects close to surface eddy current-, penetrant testing, or thermography. A high detectability of crack-like defects with X-ray radiography can however be achieved, but depends on the accessibility in order to get X-ray views in the correct angles with respect to the crack orientation.

Porosity filled with un-melted/sintered powder also represents a difficult radiographic inspection case which compared to empty or gas filled porosity produce a much lower contrast. However, the possibility to detect porosity with un-melted powder has recently been demonstrated for PBF-L samples in [52]. Therefore, in this work the defect type un-filled- and filled pore has been selected the defect of interest. The sphericity of the porosity could potentially be changed in order to make the defects similar to lack of fusion defects (both DED and PBF) and so called process-porosity (appearing in PBF). However, that has not been included in this work due to resource limitations.

The following observations have been made regarding transmission and backscatter imaging for in-situ quality control of PBD and DED:

Transmission imaging: as more of the structure is built the contrast to noise ratio for equal defects decrease, an increased difficulty and a decreased detectability is expected. The imaging mode requires that at least one view (X-ray path) through the object is accessible and practically manageable with low enough X-ray attenuation for the signal to noise ratio to be acceptable. The targeted process is the DED, since for the PBF processes only very small builds (actually the inspection limit is set by the build chamber size since the built component is embedded in powder) are assumed to be possible to inspect if fatigue critical defects are supposed to be detected.

Backscatter imaging: equal difficulty, constant contrast to noise ratio for equal defects, as more of the structure is built. The mode only requires backscattered X-ray photons to be detected and therefore a large object that cannot be penetrated with enough X-rays in any view can potentially be inspected for defects close to the inspected surface. The backscattered X-rays can be produced by for example a focused electron beam (readily available in PBF-E and electron beam DED) or by an external X-ray source (possible the electron beam in the PBF-E case can be set up as a transmission target source also, resembling the external source setup). Therefore both DED and PBF-E are the targeted processes.

In principle it would be possible to equip the process chamber of a PBF-L machine with an X-ray source and detector in order to conduct transmission or backscatter mode imaging. However, the accessibility issues seem less pronounced in the DED case and in the PBF-E case the electron beam is already present.

The transmission imaging is complicated by the fact, as stated in earlier sections, that fused and melted material is re-melted as new material is added. Since it is re-melted new defects, not present at an earlier layer or track might have sprung into existence and other might have disappeared. Therefore it cannot be assumed that the Volume V_i imaged in radiograph R is unchanged (constant defect count, sizes, and positions) when imaged together with a new volume $V_i+\Delta V$ after a new volume ΔV has been added by the operation of adding another layer or track. Initially the idea was that it could be assumed to be constant, in which case an incremental tomographic reconstruction with depth positioning could possibly be realized simply by adding projections as the build continued. Instead we propose that the change in defect count and size are to be monitored between the applied layers or tracks (depending on the projection direction). Each projection should be fully analyzed, by identifying defect indications and deriving possible defect size, position and an extended possible depth position, where depth is understood as the direction between the source and detector. The extended depth should be related to and given by the maximum possible re-melted depth between the layers. Therefore, the proposed transmission imaging setup boils down to some sort of automatic or semi-automatic algorithm for the analysis of the exposed radiographs (extraction of the defect type, size, and position). Automatic and semi-automatic analysis of radiographs is an active research area and a solution proposal for that problem is outside of the resource limits of this work.

The proposed transmission imaging procedure is illustrated in Figure 5. Two different orientations are proposed, parallel with, or perpendicular to, the build direction. In general, the detector elements close to the edge of the sample to be inspected are typically saturated, in which case the defect detectability goes to zero. The saturation is typically minimized by a mechanical mask, for example a plate is brought in close to the edge. The saturation is however only an issue in the perpendicular inspection procedure. Since in DED, the structure is typically build onto some type of substrate or component which in itself then acts as a mask. In this work, simple crude experiments in order to approximate the characteristic edge length L where the detector suffers from low defect detectability have been conducted.

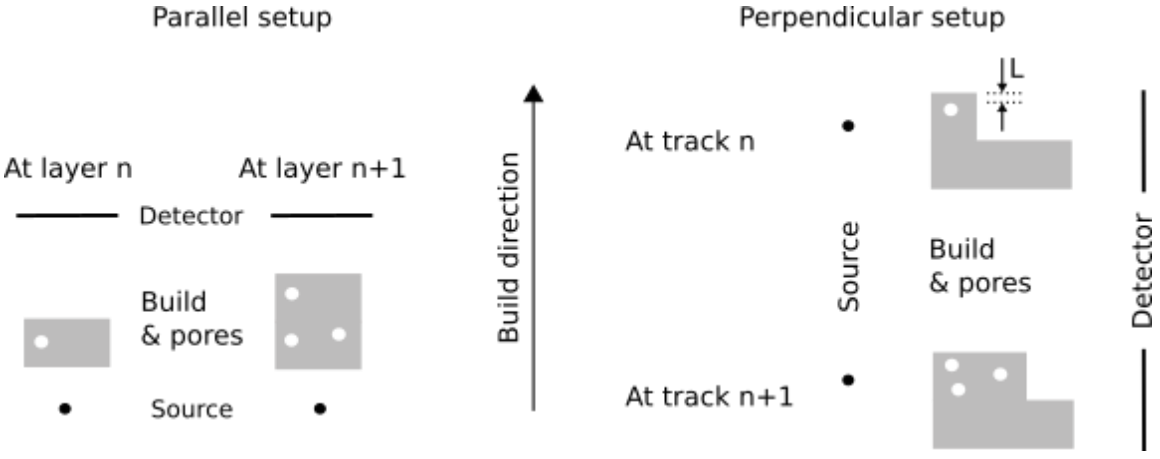

Figure 5. An illustration of the proposed setups for parallel and perpendicular in-situ transmission X-ray imaging of the DED (PBF-E if the machines is modified) process.

The proposed backscatter imaging setup and procedure is the previously described ComScan technique, see Figure 4. Since in most applications the surface roughness is at a similar characteristic length scale as the critical defects, a high resolution in the depth of the detected

defect is of interest, and a plane-by-plane imaging with an un-collimated X-ray source might be difficult to utilize. Two different X-ray sources have been considered: an electron beam (present in PBF-E) and an X-ray beam. As the electron beam or the X-ray beam impinge on the surface and the surface close bulk material it will interact with the matter in the object, after, possible numerous interactions, it might be back scattered towards the detector (see the background section for details).

It is reasonable to assume that the achievable defect resolution power of such a setup will be limited and strongly affected by the size of the interaction volume in the test object of the detected backscattered photons. In this context the interaction depth is defined as: the average distance from the surface that the detected X-ray photons interacted with the object matrix/body at. The interaction radius with respect to the center of the pencil beam of the source is also of interest and defined in the same way as the depth. The interaction depth and radius have therefore been simulated in this work for both an electron and for an X-ray beam. A ComScan similar inspection setup has also been simulated for the beam case, only if applicable based on the interaction volume, with embedded surface close pore defects.

Specific questions to be answered and the approach:

1) Is it possible to utilize the built-in electron beam in the Arcam PBF-E machines in combination with a digital X-ray detector in a backscatter X-ray imaging setup for in-situ quality control of an object built with the PBF-E process?
    a. Simulations are conducted in order to approximate the typical size of the interaction volume of the detected X-ray photons.
    b. If the interaction depth is large enough and the interaction radius small enough, simulate a backscatter X-ray radiography setup capable of detecting and resolving the depth of a small (0.1 mm) surface close (0.1-0.3 mm) pore defect.
    c. Experimentally explore if intentionally fabricated internal pore like spherical defects filled with un-melted (PBF-L) or sintered (PBF-E) powder can be detected with digital X-ray radiography. Conduct the experiments in transmission imaging mode and an X-ray tube.
2) Is it possible to utilize a robot-mounted X-ray source and digital X-ray detector in a backscatter X-ray radiography setup for in-situ quality control of an object built with a DED process?
    a. Simulations are conducted in order to approximate the typical size of the interaction volume of the detected X-ray photons.
    b. If the interaction depth is large enough and the interaction radius small enough, simulate a backscatter X-ray radiography setup capable of detecting and resolving the depth of a small (0.3 mm) surface close (0.3-1.5 mm, around three layers) pore defect.
3) Is it possible to utilize a robot-mounted X-ray source and digital X-ray detector in a transmission X-ray radiography setup for in-situ quality control of an object built with a DED process?
    a) See question 1c which is relevant also here.
    b) Experimentally explore how close to the edge pore like defects can be detected without using any mechanical (a plate) kind of edge mask.

4 Methods

4.1 Simulations

Initially the plan was to use X-ray tracing based models for the simulation of synthetic radiographs [4, 5]. However, such models are not applicable for modeling the general form of backscatter imaging which was concluded to be simulated in the project. There are applications where it is suitable to utilize the X-ray tracing models also for backscatter imaging, however this was not such an application. In applications where the scattered radiation is to be taken into account (not always but in general) Monte Carlo based simulations codes can instead be used.

There exist a large number of Monte Carlo codes for radiation transport simulation. For this project PENELOPE [54] was selected, partly because the author had previously used it. PENELOPE and its underlying models have already been validated elsewhere [55, 56]. It is capable of simulating all of the in the background listed interactions between electrons, photons, and matter in the relevant energy intervals. In addition, its source code, written in Fortran, is free and available and therefore it can easily be customized. In this work it was modified into dividing the collected signal (X-ray photons) into different radiographs depending on which interaction process the collected photons last suffered from in the test object. The possibility to calculate the previously defined interaction depth and radius for the different interaction types was also added in the code.

The principle behind the Monte Carlo approach to the simulation of radiation transport in matter is straight forward, the details are not. A number of source particles are created and tracked through a defined geometry made up of potentially different objects in different materials. The interaction of the particle with matter is random sampled, with probabilities given by so called cross sections, potentially depending on many parameters. For example in PENELOPE the cross sections are included for the elements. Alloys are then created by a weight combination of the elements. As the particle interacts with matter it will change direction, energy, might get absorbed (eventually), and create new particles. A detector object is defined where the information of interest about the collected photons is collected, for example the photon count, energy distribution, incident angle, interaction depth and radius.

It is outside the scope of this work to describe the Model Carlo simulation models in depth, for a recent review of the available implementations and models applicable for industrial X-ray radiography simulations see for example [21].

In this work only single material objects to evaluate (samples) have been considered, this is still a reasonable requirement for the selected AM processes. Three materials occur frequently in the literature review and in this work in connection to the PBF and DED processes: the titanium alloy Titan-64 (Titan-64), the nickel alloy Inconel 718, and Stainless steel 316. Each of these materials was approximated as consisting of the three elements with the highest weight per cent, according to their standards. The three materials are approximated as, the density and weight per cent composition: Titan-64, 4.4 g/cm^3, 90 % titanium, 6 % aluminium, and 4 % vanadium; Stainless steel, density 8.0 g/cm^3, 71 % iron, 17 % chromium, and 12 % nickel; Inconel, 8.8 g/cm^3, 52 % nickel, 29 % iron, and 19 % chromium. However, only Inconel and Ti64 have been simulated, since in terms of X-ray interaction Stainless steel is somewhat similar to Inconel.

4.2 Experimental setup and samples

The radiographic setup consisted of a micro focus X-ray source (Phoenix 320), with a maximum of 225 kV and 320 W, together with a digital detector array (DDA). The DDA was a small sized direct conversion dual energy photon counting DDA from XCounter (www.xcounter.se) that was borrowed to the project from the XCounter. The detector model was the entry level detector model PDT25-DE, with a pixel size of 0.1 mm^2, a dynamic range of 12 bits, and an active image area of 25.6 mm^2. A USB model with somewhat lower frame rates (sampling time) was selected for usability in this work; models with faster interfaces, larger active areas possible assembled in exotic relative arrangements can also be supplied by XCounter.

Unless otherwise stated, the source to detector distance was held fixed at 300 mm and the sample to detector distance approximately 150 mm.

The X-ray experiments were performed in GKN Aerospace Swedes's NDT lab in Trollhättan at Produktionstekniskt Centrum (Innovatum) by Erik Lindgren (KIMAB) and Peter Fridolf (GKN).

Two PBF samples were fabricated by Swerea KIMAB, see Figure 6. Both samples were fabricated to contain 10x10 pore defects, filled with un-melted/sintered powder, evenly spread out with 10 mm between each defect (total size 110x110 mm^2). Along one dimension the size of the pores was varied according to: 1, 0.8, 0.7, 0.6, 0.5, 0.4, 0.3, 0.2, 0.1, 0.05 mm; along the opposite direction the depth of the center of the pore was altered linearly from 0.5 to 5 mm. The PBF-L sample, around 10 mm thickness, was made of Stainless steel 316. The PBF-E sample, around 7.5 mm thickness, was made of Inconel 718. The existence of pore-like defects down to the size around 0.3 mm, at the sites that they were designed to be positioned, was verified with Laser ultrasonic evaluation in another project. However, the size of the defects was not characterized with the ultrasonic evaluation.

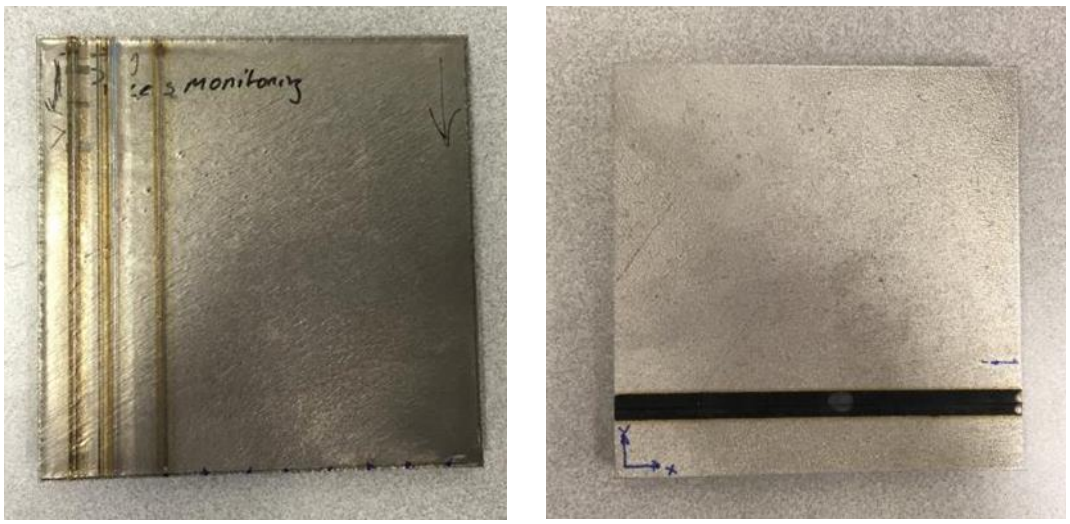

Figure 6. The PBF-E sample to the left and the PBF-L sample to the right. The dark oxide markings are from laser ultrasonic evaluation in another project.

Two samples made with DED that were plate-like in the region that was radiographed were borrowed to project from GKN Aerospace Engine Systems in Trollhättan Sweden. One wire DED-L sample around 8 mm thick which had been made with process settings to promote gas pore defects; and one powder DED-L sample around 6 mm thick with accepted quality with respect to gas porosity.

5 Results & discussion

In this section both the simulation, where most of the project resources were put, and the experimental results are presented.

5.1 Interaction depth and radius of backscattered X-rays produced by an electron beam

The objective of these simulations was to explore the possibility to utilize the already built-in electron beam in the PBF-E machines from Arcam as the X-ray source. The aim was to develop a procedure, or algorithm, for such a setup. But prior to such efforts, in this sub-section, the intrinsic limit of the detectable defect size was explored by simulating interaction depths and radiuses.

The simulated radiographic setup is shown in Figure 7. The object to detector distance (ODD) was fixed at 10 mm and the source to object distance (SOD) at 2 mm. The source was modelled as a mono-energetic zero spot size infinitely sharp electron beam (pencil beam), with its direction towards the surface of the object along the dashed line in Figure 7. The detector was modelled as energy integrating (detecting either X-ray photons or electrons) with its resolution set by the pixel sizes (0.1 mm), with a total size or 25.6 mm^2.

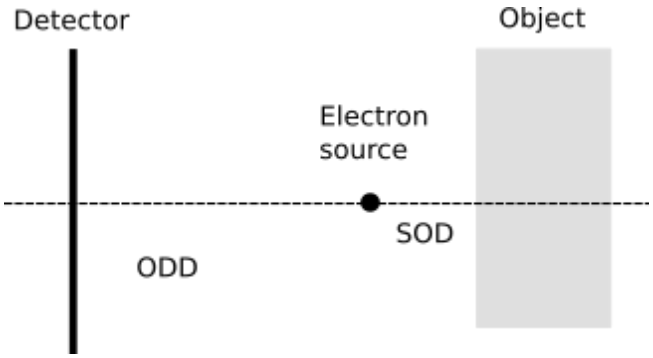

Figure 7. Illustration of the setup as modelled in PENELOPE.

As part of validating the simulation setup and the customizations of the source code (the models and software code have already been validated elsewhere [55, 56]) the backscattered and secondary electrons were detected and their penetration depths compared to literature. As can be seen in Table 1 and Table 2, in Titan-64 the interaction depth for the backscattered electrons is less than 1 µm in the selected energy range, and the interaction depth for the secondary electrons is less than 100 nm. These depths agree well the penetrations depths in textbooks on SEM, see for example [57].

Source energy [keV]	Interaction depth [nm]	Interaction radius [µm]
60	64	5
90	113	10
200	391	38
300	681	72

Table 1. Backscattered electrons in Titan-64, the simulated interaction depth and radius for different source energies, the source is an electron beam.

Source energy [keV]	Interaction depth [nm]	Interaction radius [µm]
60	8	3
90	14	6
200	40	20
300	80	38

Table 2. Secondary electrons in Titan-64, the simulated interaction depth and radius for different source energies, the source is an electron beam.

Concentrating instead on the detected X-ray photons, the interaction depths and radiuses can be seen in Table 3. The photons created by the electron beam penetrate deep enough into the material for detection of defects in the re-melted layers (around 3 layers, 200-300 µm in total). This is however only true for the photons that are scattered (Rayleigh or Compton) after created in the bremsstrahlung process. However, the scattering also decreases the intrinsic resolution considerable, as indicated with the interaction radius. In addition, only some 2-10 % of the total detected photons were scattered photons. That is, it is a rather small fraction of the detected photons that possibly do carry information about the depths of interest.

Source energy [keV]	Interaction depth [µm]		Interaction radius [µm]	
	Direct	Scattered	Direct	Scattered
60	4	44	4	94
90	8	159	9	313
200	28	729	35	1643
300	52	1205	65	2473

Table 3. The simulated interaction depth and radius of the detected bremsstrahlung X-ray photons, the source is an electron beam and the material is Titan-64. The bremsstrahlung is further divided into direct (no scattering interaction between creation and detection) and scattered (Rayleigh or Compton

scattered between creation and detection). The direct numbers had converged to less than 1 % variation and the scattered numbers to within 1-5 % variation.

The interaction depth and radius for the detected bremsstrahlung X-ray photons for the case of Inconel is shown in Table 4. The same trends as in the Titan-64 case hold. The most notable difference compared to the Titan-64 case is that for the same source energy the interaction depth and radius are lower, which is as expected.

Source energy [keV]	Interaction depth [µm]		Interaction radius [µm]	
	Direct	Scattered	Direct	Scattered
60	2	11	2	24
90	4	51	5	118
200	13	322	18	872
300	25	595	33	1417

Table 4. The simulated interaction depth and radius of the detected bremsstrahlung X-ray photons, the source is an electron beam and the material is Inconel. The bremsstrahlung is further divided into direct (no scattering interaction between creation and detection) and scattered (Rayleigh or Compton scattered between creation and detection). Both the direct and indirect numbers had converged to less than 1 % variation.

In order to improve the intrinsic resolution, by decreasing the interaction radius, two simple approaches have been explored: energy thresholding on the scattered photons and possible binning on different detector plane coordinate radius. A series of plots, each data point representing one single detected X-ray photon, see Figure 9 to Figure 13, were produced. As can be seen in Figure 8 for the Titan-64 case, the combination of an interaction depth of interest (0-300 µm) and a small interaction radius do not occur frequently but do exist. In Figure 9 and Figure 10 it is evident that no simple energy threshold would solve the intrinsic resolution issue. For example, thresholding on 20 keV would limit the radius to below 200 µm, however that would result in a too low depth at around maximum 100 µm. The possible dependence of the interaction radius and depth on the detector radius is shown in Figure 11. In Figure 12 the interaction radius and depth averaged for different detector radiuses is shown, there is some dependence on the detector radius, however the combination of a large depth and low radius is difficult to achieve. Increasing the source energy to 200 keV, see Figure 13, the correlation between the interaction radius/depth and the detector radius is stronger. However the radius is still rather large compared to the depth for a given detector radius threshold. The angle to the detector normal of the incident photon could possibly be utilized to select the combination of depth and radius of interest, but resources in the project was not left to explore that.

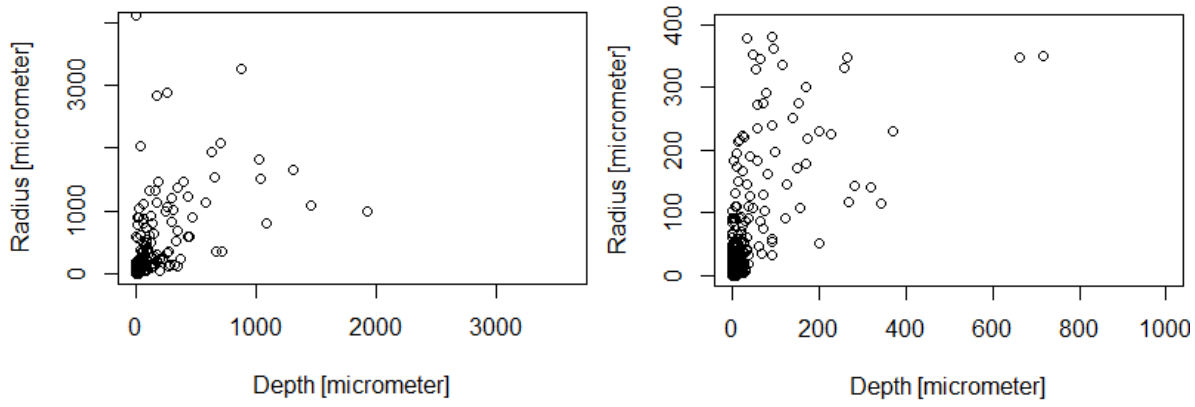

Figure 8. The simulated interaction radius versus depth for the detected scattered X-ray photons, the material is Titan-64 and the electron beam energy is 60 keV. To the right is a zoom in on the same data as displayed in the plot to the left.

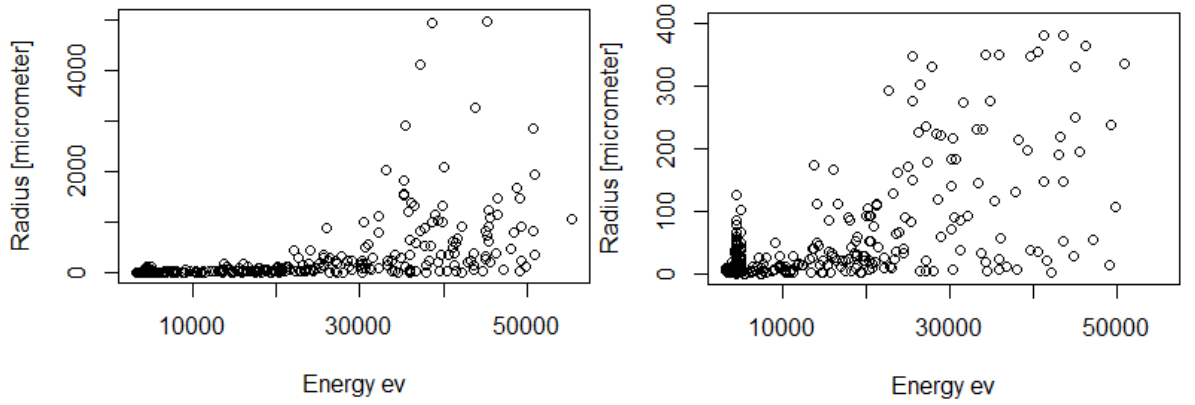

Figure 9. The simulated interaction radius versus energy for the detected scattered X-ray photons, the material is Titan-64 and the electron beam energy is 60 keV.

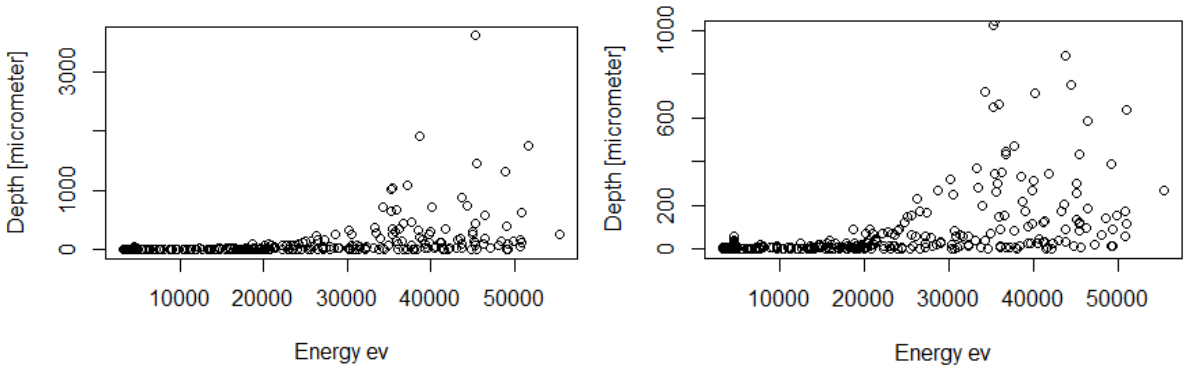

Figure 10. The simulated interaction depth versus energy for the detected scattered X-ray photons, the material is Titan-64 and the electron beam energy is 60 keV.

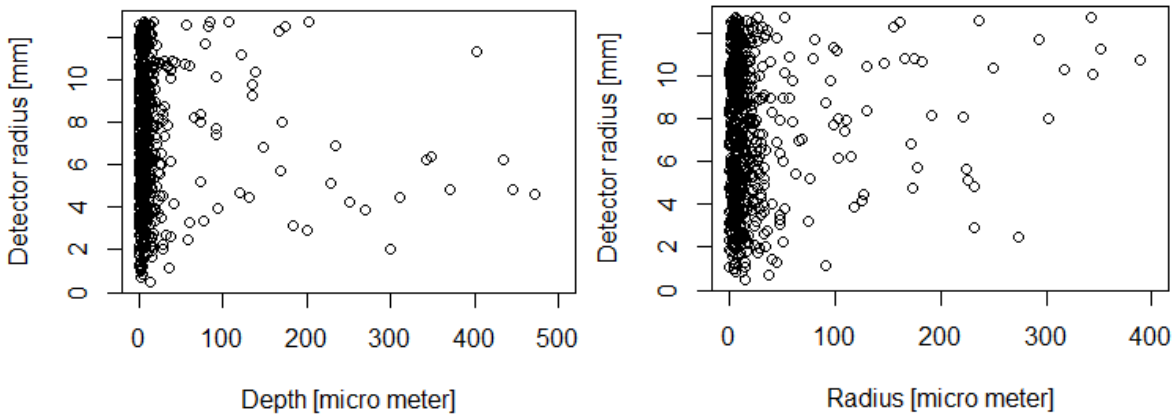

Figure 11. The simulated detector radius coordinate versus interaction depth and interaction radius for the detected scattered X-ray photons, the material is Titan-64 and the electron beam energy is 60 keV.

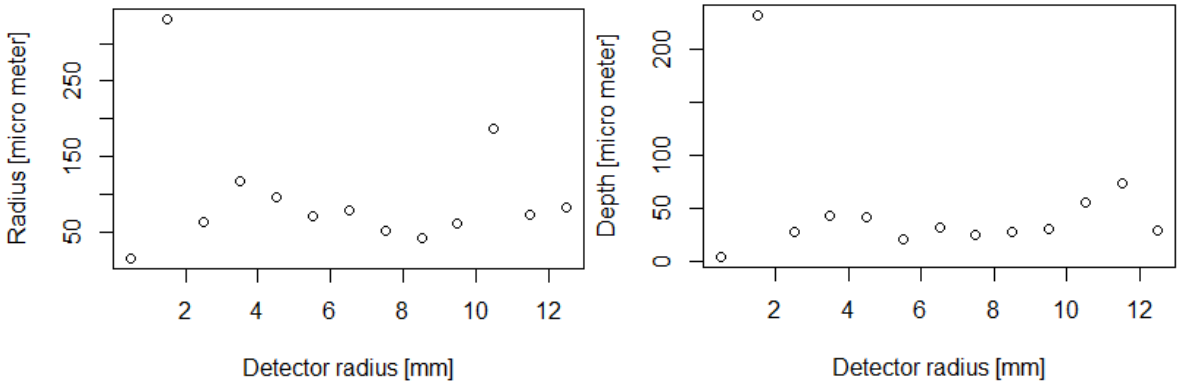

Figure 12. The simulated interaction radius and depth averaged for different detector radiuses (+/- 0.5 mm), detected X-ray photons and the material is Titan-64 and the electron beam energy is 60 keV.

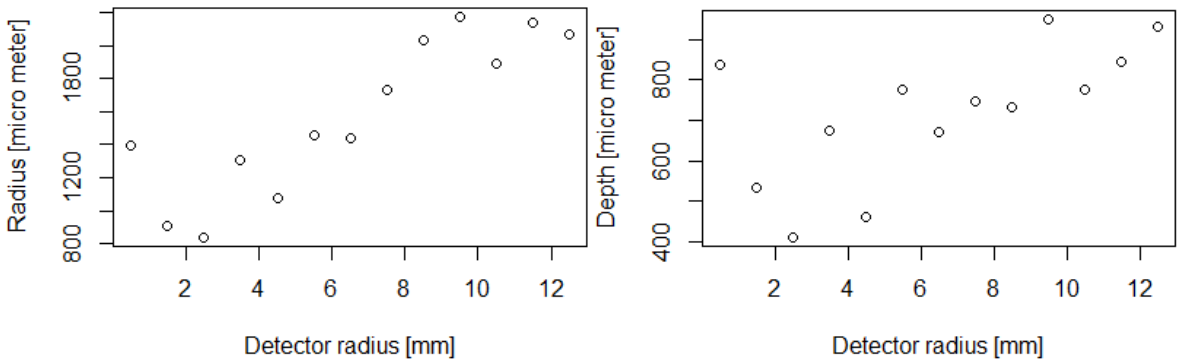

Figure 13. The simulated interaction radius and depth averaged for different detector radiuses (+/- 0.5 mm), detected X-ray photons and the material is Titan-64 and the electron beam energy is 200 keV.

5.2 Interaction depth and radius of backscattered X-rays produced by an X-ray beam

The same definitions and setup as described in the previous section was utilized to evaluate the interaction depths and radius of the detected X-ray photons produced by an X-ray beam instead of an electron beam. See figure Figure 7 in the previous section for the setup specifications.

The detected X-ray photons consisted of a mixture of mainly: coherent (Rayleigh) and incoherent (Compton) scattered photons, photons generated by photoelectric absorption and bremsstrahlung. The Compton and Rayleigh scattered dominated with total detected energy five orders of magnitude larger than both photons generated by photoelectric absorption and bremsstrahlung. The ratio between the detected and the generated number of photons was between 0.3-5 % for Titan-64 (increasing with source energy) and 0.2-4 for Inconel.

As can be seen in Table 5 and Table 6, the interaction radius is considerably smaller compared to the interaction depth, for both the Titan-64 and the Inconel sample. Therefore, the potential issue with the intrinsic low resolution in the electron beam case is not an issue in the X-ray beam case. This can be argued on since the detected photons in the X-ray beam case were mainly created in first order scattering processes, while in the electron beam case the detected photons were mostly created in higher order scattering processes. The same interaction depth in Inconel as in Titan-64 does however indicate a somewhat larger interaction radius in the Inconel case, as can be seen in Figure 14. The earlier concluded inspection depth of interest for the DED processes might be somewhere in the range 1-1.5 mm, a depth range which is thus indicated that X-ray beam photons around 70-80 keV (Titan-64) and around 120 keV (Inconel) could potentially be utilized to probe. In the values stated in both tables, the variation (standard deviation) of the average depth and radius had converged to less than 1 %.

Source energy [keV]	Interaction depth [µm]	Interaction radius [µm]
30	184	13
45	525	62
60	1022	185
90	2198	649
120	3157	1146

Table 5. The simulated backscattered X-ray photons for a Ti64 sample, the source is a pencil shaped mono-energetic X-ray beam.

Source energy [keV]	Interaction depth [µm]	Interaction radius [µm]
30	52	3
45	154	13
60	316	38
90	757	174
120	1251	422

Table 6. The simulated backscattered X-ray photons for an Inconel sample, the source is a pencil shaped mono-energetic X-ray beam.

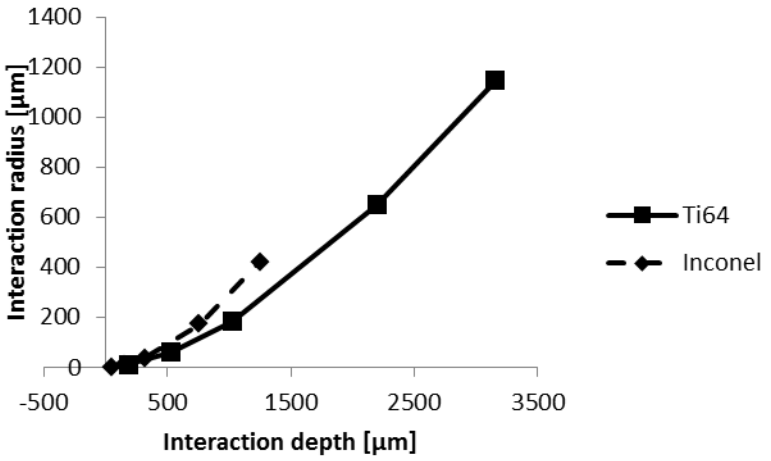

Figure 14. The simulated interaction radius and depth for the backscattered X-ray photons for the Titan-64 and the Inconel sample.

The result of calculating the average radius and depth within a 3 mm wide detector radius interval is shown in Figure 15 for the Titan-64 case. The change in depth is much less than the change in radius over the specific detector radius, the intrinsic resolution is indicated to be higher for small radiuses. However, as indicated in Figure 16 showing the total count

(energy), the contrast to noise level is expected to be optimum somewhere in the center of the selected detector radius range.

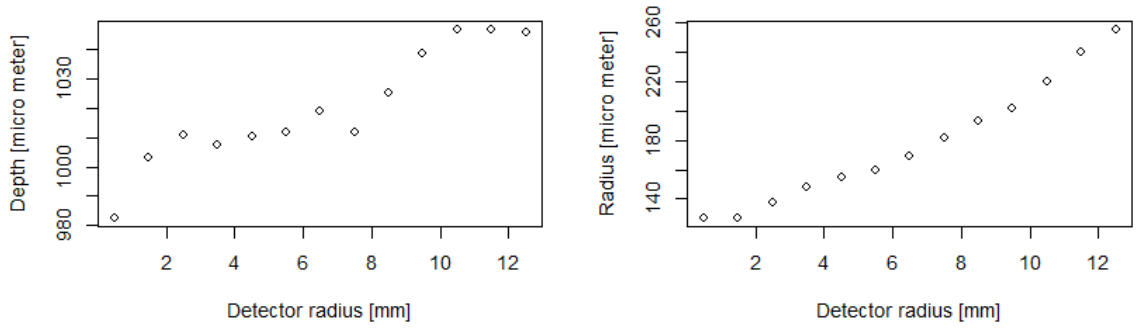

Figure 15. The simulated average interaction depth and radius versus (3 mm wide) the detector radius coordinates, Titan-64 and 60 keV X-ray beam.

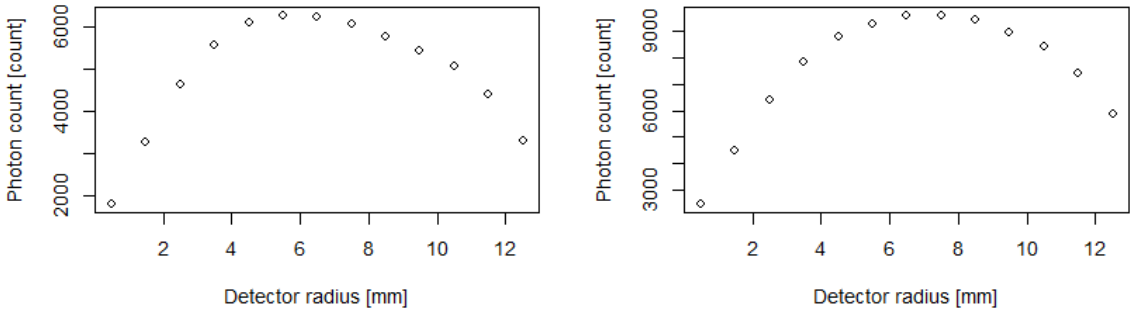

Figure 16. The simulated total detected X-ray photon count (total energy very similar) versus the detector radius coordinates, Titan-64, left) 60 keV and right) 90 keV.

The possible correlation between the interaction depth and radius with the detected photon energy was also explored. As can be seen in Figure 17, the depth does vary with the energy. However, over the energy range where there is a high photon count (required in order to get a high contrast-to-noise ratio) it does not change much. The trends are similar for the other energies in table Table 5. It should also be noted that the Compton scattered photons dominate in numbers, as they are represented by the symmetric photon count peak around 50 keV, in comparison to the Rayleigh scattered at 60 keV. The interaction radius is low around the same energy as the Compton scatter photon count peak and the Rayleigh peak. Therefore, the intrinsic resolution could potentially be somewhat maximized (though probably not much due to the low count) by detecting only photons above the energy of the start of the Compton scattering peak.

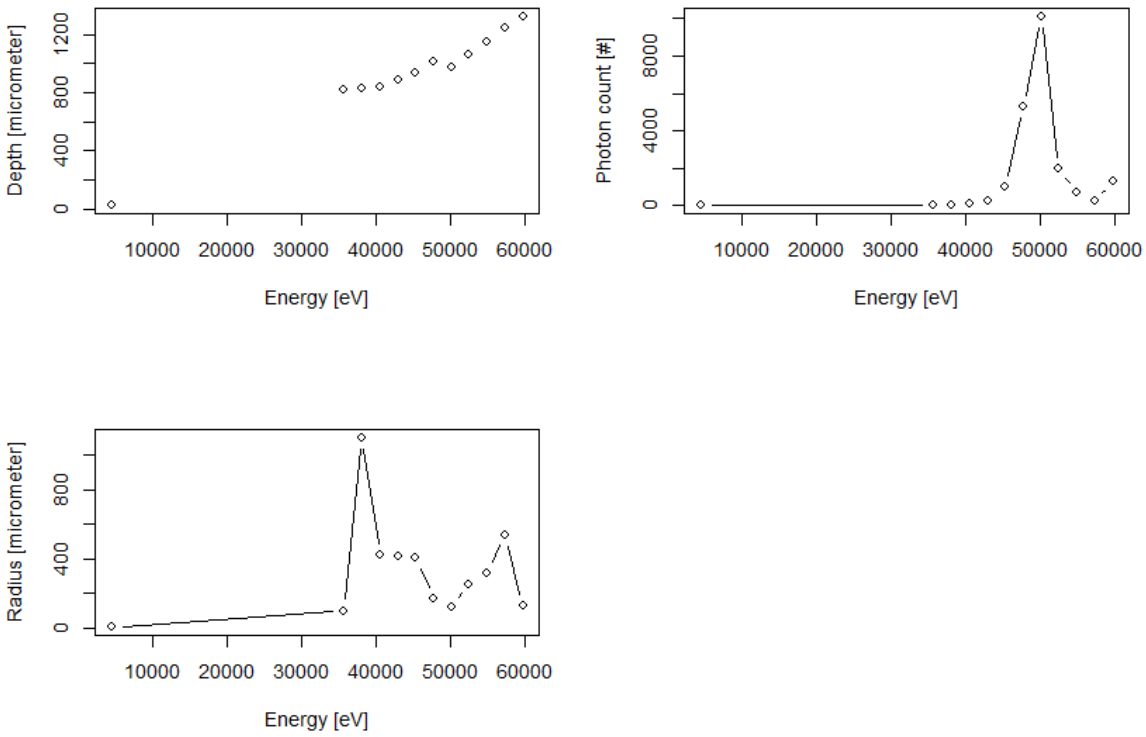

Figure 17. The simulated average depth, photon count, and radius versus energy (2.4 keV bin size), Titan-64 and 60 keV X-ray beam.

5.3 X-ray radiography with backscattered X-rays produced by an X-ray beam

An idealized setup and procedure intended for a proof of concept was set up in PENELOPE and simulated, see Figure 18. The setup was essentially the previously described ComScan setup. A single pore defect was embedded in the object at different surface to pore surface distances (depth), the material of the object was Titan-64 and the pore defect was modelled as filled with air. The thickness of the object was only 2 mm since that was the previously noted defect depth of interest (if re-done the author would choose a large thickness). A slit-collimator was positioned at a distance SOD (5 mm) from the surface of the object. The slit-collimator was modelled as an ideal lead collimator with X-ray and electron absorption energy close (59 keV) to the energy of the source (60 keV). The slit, chosen rather arbitrary as a circular pin-hole 0.1 mm in diameter, was positioned 1.5 mm above the center-line (dashed in the figure). An energy integrating detector with pixel sizes (0.1 mm) modelled as ideal (all energy deposited in a single pixel) was positioned at a distance DSD (15 mm) to the slit-collimator. A mono-energetic source at 60 keV was utilized, perfectly collimated with infinitely small spot size and with its direction centered over the pore defect.

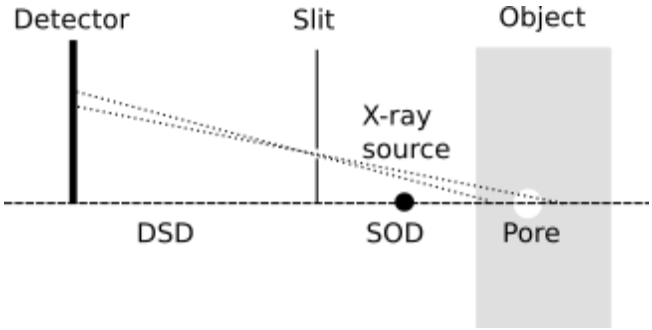

Figure 18. An illustration of the simulated X-ray backscatter imaging setup.

The detected X-ray photons originating from different depths will be detected at different height positions in the detector plane, as illustrated with dotted lines in Figure 18. The height positions can be solved for by using basic geometry and with the chosen pixel size, SOD, and DSD the depth range of around 2 mm in the object was imaged on approximately 13 pixels in the detector.

The X-ray photons collected in the detector was further separated into originating from different interactions with the object: Rayleigh and Compton scattering, the photoelectric effect, and Bremsstrahlung from secondary electrons. The total collected energy of the X-ray photons originating from the Bremsstrahlung and photoelectric effect was around 5 orders of magnitude lower than the total collected energy from the Rayleigh plus Compton scattering, and therefore of limited interest.

A limited set of three samples was simulated: no pore defect; a pore defect, 0.3 mm in diameter at a depth of 0.3 mm; a pore defect, 0.3 mm in diameter at a depth of 0.6 mm. The set was limited because the simulations were rather computation power intense. Therefore, the simulations were also parallelized and executed on a computation cluster, the Google Computing Engine (https://cloud.google.com/compute/).

The resulting simulated radiographs can be seen in Figure 19 and Figure 20. As can be seen, there is a decrease (black) in the intensity of the indication when there is a pore present, and the horizontal position of the decrease is correlated to the defect depth position. The background noise, around the indication, comes from the imperfect slit-collimator (absorption set to 59 keV) and photons created and scattered at large interaction radiuses. This was also visualized in Figure 21 with a plot of the interaction depth of the detected photons versus the detector radius coordinate. Only about a tenth of the detected photons used to produce the radiographs are included in the plot, and the background noise photons from the imperfect slit-collimator were also removed. All three simulations were run to approximately the same number of source photons (similar statistics). The ratio between the detected number of photons, related to the contrast of the indication, and the total number of source photons was only about 10^{-6}.

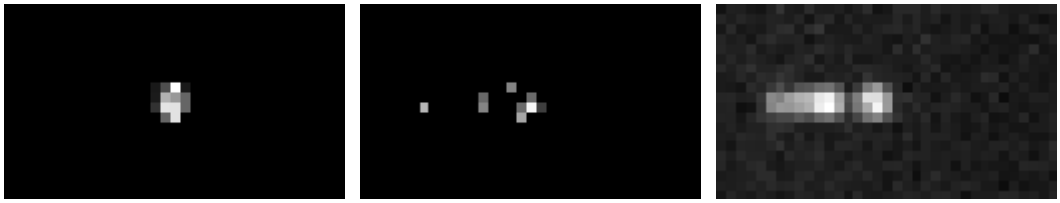

Figure 19. Simulated radiographs of a sample with a pore defect (0.3 mm diameter/0.3 mm depth), total 35 x 20 pixels selected. From the left to the right, the detected X-ray photons created by: photoelectric effect, Bremsstrahlung, and Rayleigh plus Compton scattering.

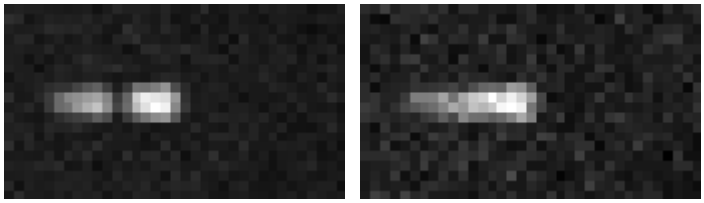

Figure 20. Simulated radiographs of a sample with: left) a pore defect (0.3 mm diameter/0.6 mm depth) and right) no pore defect. Only the radiographs of the Rayleigh plus Compton scattered X-ray photons is shown.

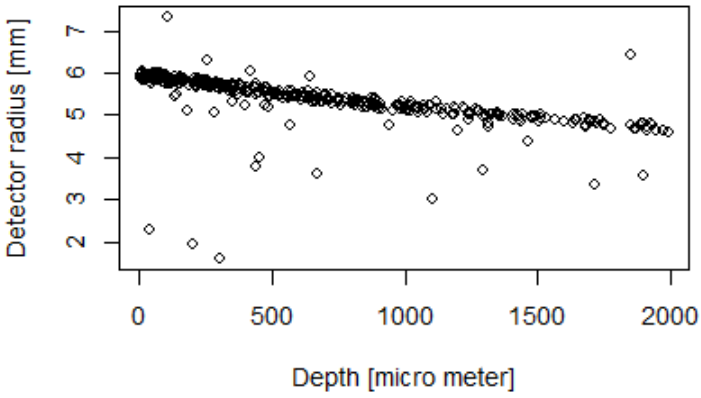

Figure 21. Detected photons, Rayleigh and Compton scattered, detector radius versus interaction depth.

The contrast of interest (indication) was also quantified with line profiles (4 pixels wide) in the horizontal direction in the Rayleigh plus Compton scattered photon radiographs, see Figure 22. The gray values in the line profiles were normalized to total number of source photons. The existence of a pore, and that it is positioned at different depths, can be seen in the line profile plot.

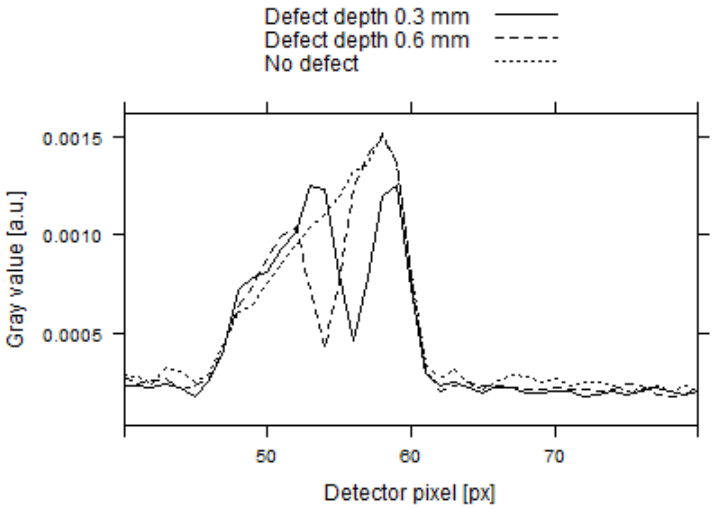

Figure 22. Line profiles (4 pixels wide) along the horizontal direction in the Rayleigh plus Compton scattered photon radiographs in Figure 19 and Figure 20. The profiles were centered over the indications.

5.4 Experimental results

5.4.1 PBF samples, printed spherical defects

Two representative experimental radiographs of the PBF-E sample can be seen Figure 23. The radiograph to the left is over a region in the sample where a 1 mm fabricated pore defect, filled with slightly sintered powder, should exist. No such indication can be identified in the radiograph. In Figure 24, the radiograph over the same sample and site but with an Inconel hole type IQI placed in front, is shown. The 1.1 mm hole in the 1.1 mm thick IQI can be identified and together with its line profile the contrast to noise ratio is indicated. Approximately two times geometrical magnification, 50 x 2 seconds of total integration time, and a tube voltage of 130 kV was utilized.

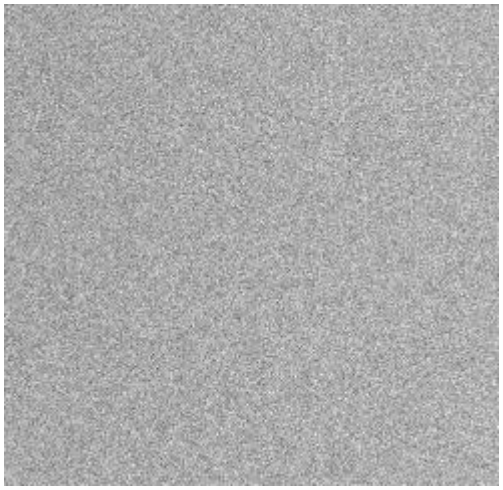

Figure 23. Radiograph of the PBF-E sample. Approximately a 10x10 mm^2 effective area over the position where a fabricated sphere filled with slightly sintered powder (diameter around 1 mm) should be present is shown.

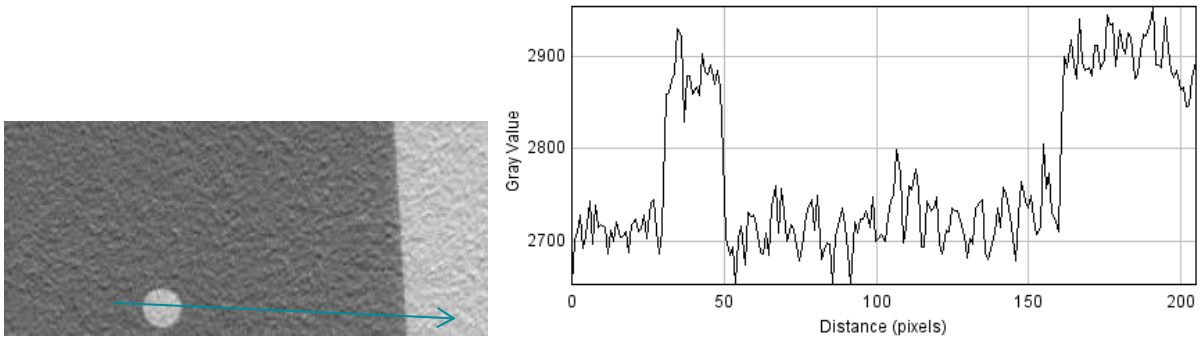

Figure 24. PBF-E, radiograph and a line profile (along the arrow line in the radiograph) over the Inconel hole IQI in the radiograph. An effective area of approximately 10x5mm^2 is imaged. In the line profile, the 1.1 mm hole is over the pixels numbered 30-50.

A representative radiograph of the PBF-L sample is shown in Figure 25. The fabricated spherical defect filled with un-melted powder is shown as the circular indication to the left in the radiograph. The size of the defect was approximated to 0.81 mm with the radiograph which is close to the design size of 0.8 mm. This should of course only be taken as an indication of the applicability of the method and is not a confident measure of its accuracy and precision. Approximately 1.5 times geometrical magnification, 50 x 2 seconds of total integration time, and a tube voltage of 120 kV was utilized.

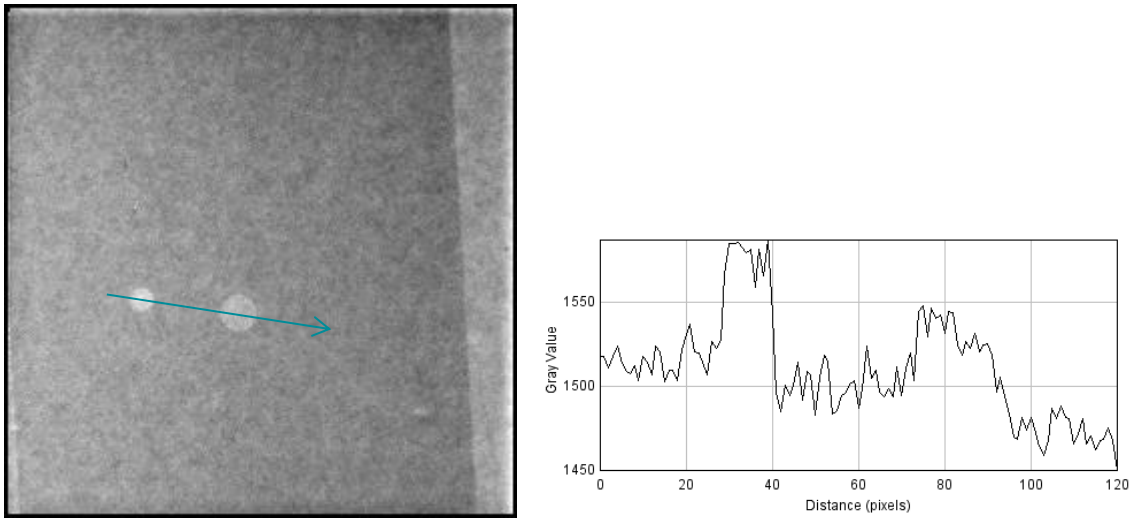

Figure 25. A radiograph of the PBF-L sample, total effective size around 10x10 mm^2. A hole type Inconel IQI is also shown in the radiograph, the thickness is 0.64 mm and the hole is 1.3 mm in diameter. Also shown is the line profile over the spherical defect and the IQI hole (arrow line in the radiograph)

The defect indication contrast is somewhat larger than the contrast of the IQI hole. It is however expected that the defect indication should be much lower in contrast than the IQI hole contrast. The hole in the 0.64 mm thick Inconel plate (higher density material than the Stainless steel in the sample but similar), should produce comparable but higher contrast than a gas pore of equal size. The fact that the spherical defect filled with un-melted powder, only 0.8/0.64 times larger, shows such a large contrast is surprising, and though the noise is considerable and conclusions should be careful, the large contrast might indicate that something is wrong. The contrast, approximated to within +/- 10 gray values, and the evaluated size of the defects (as measured in the radiographs) of 16 different exposures can be seen in Figure 26. The exposure settings were constant for all exposures, but the sample was shifted to cover many different defects and sites. The contrast values were jittered, a random number between +/- 5 gray values was added, in order to visualize the occluded data points. The trend is still evident, that the contrast difference is higher than expected, as compared to the IQI hole in Figure 25.

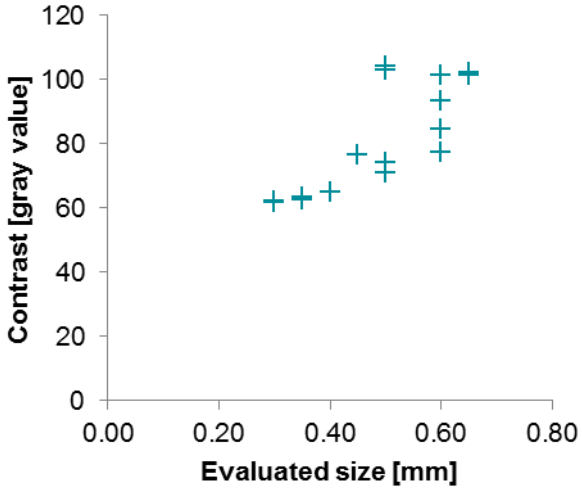

Figure 26. The contrast and the evaluated size for 16 exposures of the PBF-L sample.

5.4.2 DED samples, promoted process defects and samples of accepted quality

A radiograph of the Titan-64 wire DED-L sample with processes settings to promote porosity is shown in Figure 27. Three possible gas pore indications can be discerned, the largest was approximated to 0.3-0.4 mm in diameter. Approximately 2 times geometrical magnification, 50 x 0.26 seconds of total integration time, and a tube voltage of 120 kV was utilized.

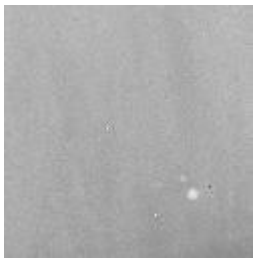

Figure 27. A radiograph of the Titan-64 wire DED-L sample, approximately 5x5mm^2 is covered in the radiograph with an effective pixel size around 0.05 mm

A radiograph of the Inconel 718 powder DED-L sample without critical pore defects is shown in Figure 28. The contrast is high enough so that the thickness/surface variation between most probable the layers can be seen as horizontal blurred linear indications separated some 0.6-0.8 mm between each other. The surface of the sample was as printed, not machined.
Approximately 2 times geometrical magnification, 100 x 0.6 seconds of total integration time, and a tube voltage of 130 kV was utilized.

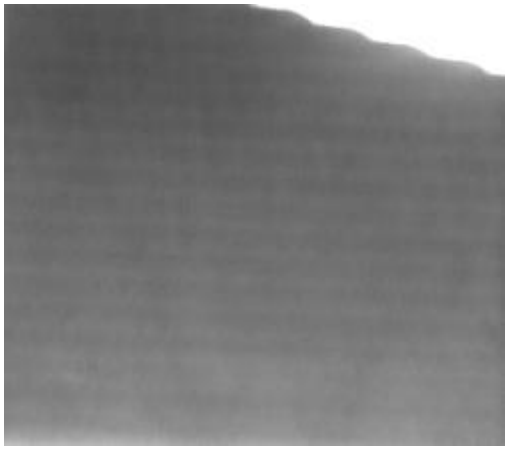

Figure 28. A radiograph of the Inconel 718 powder DED-L sample, approximately 10x8mm2 is covered in the radiograph with an effective pixel size around 0.05 mm.

5.4.3 Edge saturation

The edge saturation length for the combination of the specific utilized DDA, X-ray tube, radiographic settings and setup is indicated in Figure 29. Without much optimization, the edge length where the pixels were difficult to utilize for any defect of interest to be detected was approximated to around 7-10 pixel or 0.5 mm. The reference defect was the 0.3 mm pore defect approximated by the smallest hole in the hole type IQI in the radiograph. This should only be taken as an indication and order of magnitude approximation of the saturation length. Approximately 2 times geometrical magnification, 100 x 0.2 seconds of total integration time, and a tube voltage of 90 kV was utilized. In addition, only photons above an energy threshold of approximately 30 keV were collected in order to minimize the possible saturation from the scattered radiation at the border. This was inspired from [58] where the energy thresholding was utilized to sharpen the edges of a step wedge.

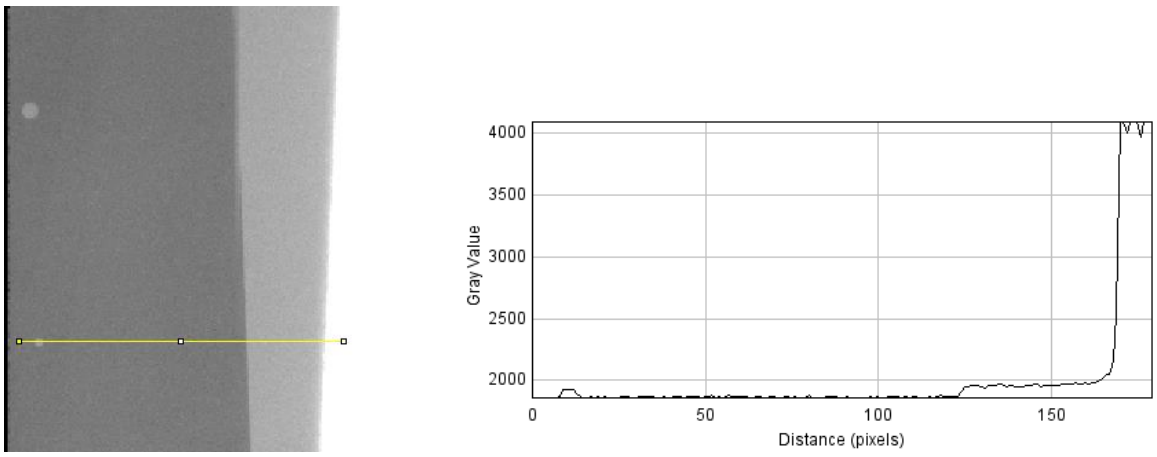

Figure 29. A radiograph of a 0.3 mm thick Titan-64hole IQI over a 4.7 mm thick Titan-64 plate. To the right is the line profile shown along the yellow line that is indicated in the radiograph.

6 Conclusions

Mathematical models of the interaction of X-rays with matter have been utilized in order to develop concepts and techniques for in-situ nondestructive evaluation of 3D printed metal components. Both transmission and backscatter X-ray imaging have been considered with emphasis on backscatter imaging. To the authors best knowledge no such scientific publications on utilizing such X-ray inspection for this application is known, though similar approaches for inspection of cladding processes have been published.

Based on other potential nondestructive evaluation methods it was proposed that the defect of interest to detect and characterize with an X-ray radiography method would be void defects, un-filled/air or filled with un-melted/sintered powder.

Simulations of the interaction depth and radius of the detected backscattered X-ray photons produced by an electron beam (already available in the for example PBF-E machines) was indicated to result in a too low intrinsic lateral resolution for the proposed defects of interest in the size range 100 µm. Similar simulations but with the backscattered X-rays produced by an external X-ray source (in for example DED-L machines) was indicated to result in a possible good enough intrinsic resolution for the selected defects.

A proposed backscatter X-ray imaging procedure and setup (based on an external X-ray source) capable of detection and depth positioning of the surface close defects was successfully simulated. The electron beam in the PBF-E machine can possible be set up to operate as a transmission target X-ray tube with a collimator built into the target (perhaps being the actual target). In such a case, the setup would be equivalent to the simulated X-ray beam case.

In addition to the backscatter imaging concepts, transmission imaging was also proposed as a setup possible suitable for the DED processes. The problem was transformed mostly into the research on automatic and semi-automatic analysis of the X-ray radiographic evaluation. Simple experiments were conducted to estimate the issue with detector pixel saturation close to edges which could be a potential problem in a specific set of transmission X-ray imaging setups.

In addition, experiments in transmission mode evaluation of PBF-L, PBF-E, and powder and wire DED-L samples were conducted. Backscatter imaging would have been more interesting to explore, however, resources in the project was not enough for that. The radiographic contrast was verified to be large enough to detect: real gas porosity defects (approximately 0.3-0.4 mm) in a wire DED-L sample; intentionally made spherical defects (as small as 0.3 mm) filled with un-melted powder in Stainless steel 316 PBF-L samples. The intentionally fabricated spherical defects filled with sintered powder in Inconel 718 PBF-E samples could not be detected. During the PBF-E sample exposures there were some practical issues with the positioning and calibration. Therefore, the results should not be interpreted as a proof of the detectability of the defects filled with sintered powder.

Some form of scanning of the X-ray detector and source is required and even though the time of the measurement could potentially be large, the evaluation might for example be useful during process development (new AM machines, new powder materials, and so on).

7 Acknowledgments

The financial support from ÅForsk Foundation (grant 16-514) and from the Swedish state (basic funding, strategic competence development, to the research institute Swerea KIMAB) is acknowledged.

GKN Aerospace Sweden is acknowledged for supplying directed energy deposition samples and for access to their research and development X-ray lab in Trollhättan, as well as for practical help with the X-ray experiments.

XCounter is acknowledged for lending one of their digital detector arrays to the project.

Joakim Ålgårdh is acknowledged for reviewing the parts on additive manufacturing as well as for producing the powder bed fusion samples together with Jesper Vang, both at Swerea KIMAB.

8 References

[1] E. Lindgren. Detection, 3-d positioning, and sizing of small pore defects using digital radiography and tracking. *EURASIP Journal of Advances in Signal Processing*, 2014: 9, 2014.

[2] E. Lindgren. Detection and 3-d positioning of small defects using 3-d point reconstruction, tracking, and the radiographic magnification technique. *NDT & E International*, 76: 1–8, 2015.

[3] G.-R. Tillack, U. Samadurau, V. Artemiev, and A. Naumov. Statistical characterization of multi-phase flow by dynamic tomography. In *Review of Quantitative Nondestructive Evaluation*, volume 22, pages 643–650, 2003.

[4] C. Bellon, A. Deresch, C. Gollwitzer, and G.-R. Jaenisch. Radiographic simulator artist: Version 2. In *18th World Conference on Nondestructive Testing*, 2012.

[5] E. Lindgren and H. Wirdelius. X-ray modeling of realistic synthetic radiographs of thin titanium welds. *NDT & E International*, 51: 111–119, 2012.

[6] I. Gibson, D. Rosen, and B. Stucker. *Additive Manufacturing Technologies*. Springer, 2015.

[7] J. Karlsson. *Optimization of Electron Beam Melting for Production of Small Components in Biocompatible Titanium Grades*. PhD thesis, Uppsala Universitet, 2015.

[8] J. Sundström. Additive manufacturing of ni-based superalloys, state-of-the-art review. Technical report KIMAB-2016-154, Swerea KIMAB, 2016.

[9] M. Ramsperger, R.F. Singer, and C. Körner. Microstructure of the nickel-base superalloy cmsx-4 fabricated by selective electron beam melting. *Metallurgical and Materials Transactions A*, 47 (3): 1469–1480, Mar 2016. ISSN 1543-1940.

[10] A. Strondl, M. Palm, J. Gnauk, and G. Frommeyer. Microstructure and mechanical properties of nickel based superalloy in718 produced by rapid prototyping with electron beam melting (ebm). *Materials Science and Technology*, 27: 876–883, 2011.

[11] W.J. Sames, F. Medina, W.H. Peter, S.S. Babu, and R.R. Dehoff. *Effect of Process Control and Powder Quality on Inconel 718 Produced Using Electron Beam Melting*, pages 409–423. John Wiley & Sons, Inc., 2014. ISBN 9781119016854.

[12] W.J. Sames. *Additive Manufacturing of Inconel 718 using Electron Beam Melting: Processing, Post-processing, and Mechanical Properties*. PhD thesis, Texas A&M University, 2015.

[13] G. Kasperovich, J. Haubrich, J. Gussone, and G. Requena. Correlation between porosity and processing parameters in tial6v4 produced by selective laser melting. *Materials & Design*, 105 (Supplement C): 160 – 170, 2016. ISSN 0264-1275.

[14] L. Rickenbacher, T. Etter, S. Hövel, and K. Wegner. High temperature material properties of in738lc processed by selective laser melting (slm) technology. *Rapid Prototyping Journal*, 19: 282–290, 2013.

[15] M. Cloots, P. J. Uggowitzer, and K. Wegener. Investigations on the microstructure and crack formation of in738lc samples processed by selective laser melting using gaussian and doughnut profiles. *Materials and Design*, 89: 770–784, 2016.

[16] P.A. Kobryn, E.H. Moore, and S.L. Semiatin. The effect of laser power and traverse speed on microstructure, porosity, and build height in laser-deposited to-6al-4v. *Scripta mater.*, 43: 299–305, 2000.

[17] G.K. Lewis and E. Schlienger. Practical considerations and capabilities for laser assisted direct metal deposition. *Materials and Design*, 21: 417–423, 2000.

[18] M. Leino, J. Pekkarinen, and R. Soukka. The role of laser additive manufacturing methods of metals in repair, refurbishment and remanufacturing - enabling circular economy. *Physics Procedia*, 83: 752–760, 2016.

[19] B. Graf, A. Gumenyuk, and M. Rethmeier. Laser metal deposition as repair technology for stainless steel and titanium alloys. *Physics Procedia*, 39: 376–381, 2012.

[20] Peter J. Shull, editor. *Nondestructive Evaluation*. M. Dekker, 2002.

[21] E. Lindgren. *Detection and 3-D positioning of small defects using digital radiography, 3-D point reconstruction, and tracking*. PhD thesis, Chalmers University of Technology, 2015.

[22] N.A. Dyson. *X-ray in atomic and nuclear physics*. Cambridge University Press, 1990.

[23] G. Harding and E. Harding. Compton scatter imaging: A tool for historical exploration. *Applied Radiation and Isotopes*, 68: 993–1005, 2010.

[24] D. Babot, G. Berodias, and G. Peix. Detection and sizing by x-ray compton scattering of near-surface cracks under weld deposited cladding. *NDT & E International*, 24 (5): 247 – 251, 1991. ISSN 0963-8695.

[25] P. Zhu, P. Duvauchelle, G. Peix, and D. Babot. X-ray compton backscattering techniques for process tomography: imaging and characterization of materials. *Measurement Science and Technology*, 7: 281–286, 1996.

[26] S. Naito and S. Yamamoto. Novel x-ray backscatter technique for detecting crack below deposit. In *7th International Conference on NDE in Relation to Structural Integrity for Nuclear and Pressurized Components*, 2010.

[27] S. Kolkoori, N. Wrobel, U. Zscherpel, and U. Ewert. A new x-ray backscatter imaging technique for non-destructive testing of aerospace materials. *NDT&E International*, 70: 41–52, 2015.

[28] F. Wieder, U. Ewert, J. Vogel, G.-R. Jaenisch, and C. Bellon. A novel multi slit x-ray backscatter camera based on synthetic aperture focusing. In *Review of Progress in Quantitative Nondestructive Evaluation*, volume 1806 of *AIP Conference Proceedings*, page 130002, 2017.

[29] S. Everton, M. Hirsch, P. Stravroulakis, R. Leach, and A. Clare. Review of in-situ process monitoring and in-situ metrology for metal additive manufacturing. *Materials and Deign*, 95: 431–445, 2016.

[30] S. Clijsters, T. Craeghs, S. Buls, K. Kempen, and J.-P. Kruth. In situ quality control of the selective laser melting process using a high-speed, real-time melt pool monitoring system. *Int J Adv Manuf Technol*, 75: 1089–1101, 2014.

[31] S. Moylan, E. Whitenton, B. Lane, and J. Slotwinski. Infrared thermography for laser-based powder bed fusion additive manufacturing process. In *Review of Progress in Quantitative Nondestructive Evaluation*, volume 1581 of *AIP Conference Proceedings*, pages 1191–1196, 2014.

[32] C. Volker. Monitoring system for the quality assessment in additive manufacturing. In *Review of Progress in Quantitative Nondestructive Evaluation*, volume 1650 of *AIP Conference Proceedings*, pages 171–176, 2015.

[33] B. Lane, S. Moylan, E.P. Whitenton, and L. Ma. Thermographic measurements of the commercial laser powder bed fusion process at nist. *Rapid Prototyping Journal*, 22 (5): 778–787, 2016.

[34] R. Dinwiddie, R. Dehoff, P. Lloyd, L. Lowe, and J. Ulrich. Thermographic in-situ process monitoring of the electron beam melting technology used in additive manufacturing. In *Thermal Infrared Applications*, volume 8705 of *Proc. of SPIE*, 2013.

[35] H. Krauss, T. Zeugner, and M. Zaeh. Thermographic process monitoring on powderbed based additive manufacturing. In *Review of Progress in Quantitative Nondestructive Evaluation*, volume 1650 of *AIP Conference Proceedings*, pages 177–183, 2015.

[36] J. Krautkrämer and H. Krautkrämer. *Ultrasonic Testing of Materials*. Springer-Verlag, 1990.

[37] C.B. Scruby and L.E. Drain. *Laser Ultrasonics Techniques and Applications*. CRC Press, 1990.

[38] H. Rieder, A. Dillhöfer, M. Spies, J. Bamberg, and T. Hess. Online monitoring of additive manufacturing process using ultrasound. In *11th European Conference on Non-Destructive Testing (ECNDT 2014)*, 2014.

[39] J. A. Slotwinski and E. J. Garboczi. Porosity of additive manufacturing parts for process monitoring. In *Review of Progress in Quantitative Nondestructive Evaluation*, volume 1581 of *AIP Conference Proceedings*, pages 1197–1204, 2014.

[40] M. Klein and J. Sears. Laser ultrasonic inspection of laser cladded 316lss and ti-6-4. In *Proceedings of the 23rd International Congress on Applications of Lasers and Electro-Optics 2004*, 2004.

[41] J. Rudlin, D. Cerneglia, M. Scafidi, and C. Schneider. Inspection of laser powder deposited layers. In *11th European Conference on Non-Destructive Testing (ECNDT 2014)*, 2014.

[42] D. Levesque, C. Bescond, M. Lord, X. Cao, P. Wanjara, and J.-P. Monchalin. Inspection of additive manufactured parts using laser ultrasonics. In *Review of Progress in Quantitative Nondestructive Evaluation*, volume 1706 of *AIP Conference Proceedings*, pages 1300031–1300039, 2016.

[43] D. Levesque, A. Blouin, C. Neron, and J.-P. Monchalin. Performance of laser-ultrasonic f-saft imaging. *Ultrasonics*, 40: 1057–1063, 2002.

[44] D. Cerneglia, M. Scafidi, A. Pantano, and J. Rudlin. Inspection of additive-manufactured layered components. *Ultrasonics*, 62: 292–298, 2015.

[45] S. Everton, P. Dickens, C. Tuck, and B. Dutton. Evaluation of laser ultrasonic testing for inspection of metal additive manufacturing, 2015.

[46] S. K. Everton, P. Dickens, C. Tuck, and B. Dutton. Identification of sub-surface defects in parts produced by additive manufacturing using laser generated ultrasound. In *Materials Science and Technology Conference and Exhibition 2016*, volume 1, pages 141–148, 2016.

[47] D. Clark and D.C. Wright. Methods of and apparatus for producing an object or structure including testing and/or analysing of objects and structures, August 8 2007. EP Patent App. EP20,070,250,067.

[48] A. Thompson, I. Maskery, and R. Leach. X-ray computed tomography for additive manufacturing: A review. *Measurement Science and Technology*, 27: 072001, 06 2016.

[49] S. Carmignato. Accuracy of industrial computed tomography measurements experimental results from an international comparison. *CIRP Annals - Manufacturing Technology*, 61: 491–494, 2012.

[50] P. Hermanek and S. Carmignato. Reference object for evaluating the accuracy of porosity measurements by x-ray computed tomography. *Case Studies in Nondestructive Testing and Evaluation*, 6 (Part B): 122 – 127, 2016. ISSN 2214-6571.

[51] A. Jansson, A. R. Zekavat, and L. Pejryd. Measurement of internal features in additive manufactured components by the use of computed tomography. In *Digital Industrial Radiology and Computed Tomography (DIR 2015)*, 2015.

[52] P.A. Rometsch, D. Pelliccia, D. Tomus, and X. Wu. Evaluation of polychromatic x-ray radiography defect detection limits in a sample fabricated from hastelloy x by selective laser melting. *NDT & E International*, 62 (Supplement C): 184 – 192, 2014. ISSN 0963-8695.

[53] P. Nilsson, A. Appelgren, P. Henrikson, and A. Runnemalm. Automatic ultrasonic testing for metal deposition. In *18th World Conference on Nondestructive Testing*, 2012.

[54] F. Salvat, J.M. Fernandez-Varea, and J. Sempau. Penelope-2008: A code system for monte carlo simulation of electron and photon transport. Technical report, OECD ISBN 978-92-64-99066-1, 2008.

[55] J. Sempau, J.M. Fernandez-Varea, E. Acosta, and F. Salvat. Experimental benchmarks of the monte carlo code penelope. *Nuclear Instruments and Methods in Physics Research B*, 207: 107–123, 2003.

[56] J. Baro, M. Roteta, J.M. Fernandez-Varea, and F. Salvat. Analytical cross sections for monte carlo simulation of photon transport. *Radiation Physics and Chemistry*, 44: 531–552, 1994.

[57] Y. Leng. *Materials Characterization Introduction to Microscopic and Spectrscopic Methods*. Wiley-VCH, 2013.

[58] U. Zscherpel, D. Walter, B. Redmer, U. Ewert, C. Ullberg, N. Weber, and T. Pantzar. Digital radiology with photon counting detectors. In *11th European Conference on Non-Destructive Testing (ECNDT 2014)*, 2014.

swerea | KIMAB
Box 7047, 164 07 Kista, Sweden
Visiting Isafjordsgatan 28 A, 164 40 Kista, Sweden
+46 8 440 48 00, kimab@swerea.se, www.swereakimab.se